Doelesso, A. E., Dupont-Nivet, G., Kidane, T., Nowaczyk, N., Sudo, M., Melnick, D., Bookhagen, B., Brune, S., Corti, G., Gecho, G., Strecker, M. (2025): Temporal variation in counterclockwise vertical-axis block rotations across a rift overlap zone, southwestern Ethiopia, East Africa. - Tectonophysics, 897, 230599.

https://doi.org/10.1016/j.tecto.2024.230599

Temporal variation in counterclockwise vertical-axis block rotations across a rift overlap zone, southwestern Ethiopia, East Africa

A. Erbello[1,2], G. Dupont-Nivet[3,5], T. Kidane[4], N. Nowaczyk[5], M. Sudo[1], D. Melnick[6], B. Bookhagen[1], S. Brune[5,1], G. Corti[7], G. Gecho[8], and M.R. Strecker[1]

[1]Institute of Geosciences, University of Potsdam, Potsdam, Germany.

[2]Now at Applied Geology Department, School of Natural Sciences, Adama Science and Technology University, Adama, Ethiopia.

[3]Géosciences Rennes, UMR 6118, Université de Rennes 1, Rennes, France.

[4]Environmental Science and Geology Department, College of Liberal Arts and Sciences, Wayne State University, USA.

[5]Helmholtz Centre Potsdam-GFZ German Research Centre for Geosciences, Potsdam, Germany.

[6]Instituto de Ciencias de la Tierra, Universidad Austral de Chile, Valdivia, Chile

[7]Consiglio Nazionale delle Ricerche, Istituto di Geoscienze e Georisorse, Firenze, Italy.

[8]Arba-Minch University, College of Natural and Computational Sciences, Geology Department, Arba-Minch, Ethiopia.

Corresponding author: Asfaw Erbello (asfaw.erbello@astu.edu.et, asfaw.erbello.doelesso@uni-potsdam.de)

Highlights:

- Paleomagnetic results from the extensional overlap zone of the Gidole plateau between the southern Main Ethiopian Rift and the Chew Bahir-Gofa Province reveal counterclockwise vertical-axis rotations.
- The extent of the vertical-axis block rotations progressively decreased from Oligocene to Miocene following the regional patterns of deformation.
- The deformation associated with the vertical-axis block rotations was likely associated with the reactivation of inherited NW-SE-striking basement fabrics.

Abstract

The southward propagation of the southern Main Ethiopian Rift (sMER) and the northward propagation of the Kenya Rift have generated the Broadly Rifted Zone (BRZ), a ~40-km-wide region of extensional overlap between the Chew Bahir Basin-Gofa Province and the sMER. However, the tectonic interaction between these propagating rifts is not well-understood. We present new paleomagnetic and geochronologic data from Eo–Oligocene (45–35 Ma) and Miocene (18–11 Ma) volcanic and sedimentary rocks from the BRZ. Rock magnetic, alternating field and thermal demagnetization experiments indicate simple titanomagnetite mineralogies carrying a characteristic remanent magnetization from which straightforward magnetization directions were obtained. Site-mean paleomagnetic directions obtained from the analyzed samples reflect stable normal and reversed polarity directions. A comparison of the mean directions obtained for the Eo–Oligocene and Miocene rocks relative to the pole for stable South Africa at the corresponding ages reveals a significant counterclockwise (CCW) rotation of ~11.1° ± 6.4° and insignificant CCW rotation of ~3.2° ± 11.5°, respectively, reflecting a decrease in the extent of block rotations through time. Our results are consistent with the regional migration patterns of deformation during rifting. In the context of the regional tectonic evolution toward a narrow zone of extension, much of the deformation associated with block rotations probably occurred prior to the final stages of the emplacement of the Miocene volcanic flows. In light of the structural fabrics in the basement rocks exposed in the sMER, the observed CCW block rotations were likely accompanied and aided by the reactivation of NW-SE-striking basement heterogeneities, supporting the notion that inherited crustal-scale structures play a significant role during rifting across the BRZ.

1 Introduction

Continental rifts are nascent extensional plate boundaries and commonly evolve from the growth of normal-fault bounded, initially isolated basins to linked graben systems, and ultimately ocean basins (e.g., Ebinger et al., 1999; Ebinger and Scholz, 2012 and references therein). In map view, these fault-bounded basins are often laterally separated from each other. A lateral transfer of extensional strain between these basins is thus required over time to kinematically link these different sites of tectonic subsidence and extension and to maintain crustal extension between spatially disparate rift segments (e.g., Rosendahl, 1987; Childs et al., 1993, 1995). The structural character of rift-transfer zones may be further complicated either when the transfer of strain is associated with the reactivation of inherited crustal-scale heterogeneities or if rotations are involved to accommodate the differential motion of crustal blocks (e.g., Bosworth 1985; Rosendahl et al., 1987; Morley et al., 1990, 1992; Dawers and Anders, 1995; Peacock, 2002; Hetzel and Strecker, 1994; Bosworth, 1992; Corti, 2008;). The topographic relief patterns of such transfer zones may exert a crucial influence not only on the dispersal patterns of biota and thus on biodiversity (e.g., Dommain et al., 2022), but also on the evolution of the hydrological network and sediment transport as well as on the permeability and fluid flow along individual structures (e.g., Morley et al., 1990; Nelson et al., 1992; Morley et al., 1994; Garcin et al., 2012; Dommain et al., 2022; Olaka et al., 2022).

Therefore, characterizing and understanding the kinematics of faults in transfer zones, also known as accommodation zones (e.g., Rosendahl et al., 1987), is an important step in identifying the individual stages of rift evolution and the environmental impact of fault systems, especially at the termination of rift segments and within their transfer zones. One of the tectonically active extensional regions where different types and spatial scales of rift-transfer zones can be best observed at various evolutionary stages is the Cenozoic East African Rift System (EARS). Along strike, the EARS comprises several propagating rift segments that interact via complex transfer faults, often characterized by wide zones of diffuse deformation

(e.g., Rosendahl et al., 1987; Morley, 1992; Ebinger et al., 1999; Koehn et al., 2008; Brune et al., 2017; Corti et al., 2019; Kolawole et al., 2021).

With a length of ~2000 km, the EARS extends from the Afar depression in the north to Malawi and Mozambique in the south; in the Turkana depression it bifurcates into an eastern and a western branch (Fig.1a). The eastern branch, comprising the southern Afar, Main Ethiopian and Kenya rifts, is characterized by pronounced volcano-tectonic processes, whereas the western branch is volcanically less active (Fig. 1a). Geological and geophysical data from the western and eastern branches indicate that many of the adjacent rift segments are linked by transfer faults (e.g., Kolawole et al., 2021); often, fault motion within such transfer zones is influenced by inherited structures related to earlier deformation processes (e.g., Versfelt and Rosendahl, 1989; Brune et al., 2017; Corti et al., 2019). In contrast, other transfer zones in the EARS are characterized by a wide area of overlap between propagating strands of normal faults (e.g., Morley, 1994, Ebinger et al., 1999; Acocella, 2005).

Based on paleomagnetic, geodetic, seismic data, and mechanical modeling results, microplate rotations between overlapping rift segments have been inferred from different sectors in the EARS and the Afar Rift (e.g., Acton et al., 1991; Kidane et al., 2003, 2009; Koehn et al., 2008; Saria et al., 2013, 2014; Muluneh et al., 2014; Nugsse et al., 2018; Philippon et al., 2014; Brune et al., 2017; Glerum et al., 2020). While in the northern Main Ethiopian and southern Afar rifts, Kidane et al. (2003), Muluneh et al. (2014), and Nugsse et al. (2018) inferred a counterclockwise block rotation in an extensional zone located between right-stepping Quaternary magmatic segments, such paleomagnetic studies from the southern Main Ethiopian Rift, the Broadly Rifted Zone (BRZ), and farther south in the Kenya Rift and western branch of the EARS, are not available. Continuous geodetic measurements along and across the EARS indicate that the Ufipa microplate located between the left-stepping structures of the Rukwa and Tanganyika rifts (Fig. 1b) is rotating in a clockwise direction (Calais et al., 2006; Fernandes et al., 2013; Deprez et al., 2013; Saria et al., 2013, 2014; Stamps et al., 2008, 2018, 2021).

Farther north in the western branch of the EARS, numerical and analog modeling of extensional structures (e.g., Koehn et al., 2008; Ayue and Koehn; 2010) have also indicated a clockwise rotation of the Rwenzori microplate, which is located between the left-stepping structures that delimit the Edward and Albert rifts (Fig. 1c). Similarly, counterclockwise rotation involving reactivated Mesozoic crustal anisotropies affects an uplifted crustal block between right-stepping rift segments of the Chew Bahir-Gofa Province and the southern Main Ethiopian rift (e.g., Philippon et al., 2014; Brune et al., 2017; Sullivan et al., 2024). Finally, and at a much larger spatial scale, a counterclockwise rotation of a mechanically strong, undeformed layer of the Victoria microplate located between the right-stepping eastern and western branches of the EARS was inferred by Glerum et al. (2020) (Fig. 1d). These findings show that the type of rift overlap (right- or left-stepping) controls the direction of microplate rotation across all relevant scales because the geometric relationship between stepover and rotation is scale-invariant (McKenzie and Jackson, 1986; Schouten et al., 1993; Katz et al., 2005; Koehn et al., 2010; Glerum et al., 2020).

Taken together, the inferred microplate rotations between the propagating structures of the Rukwa and Tanganyika rifts (Ufipa Horst), the Edward and Albert rifts (Rwenzori microplate), the eastern and western branches of the EARS (Victoria microplate), and between the southern Main Ethiopian Rift and the Chew Bahir-Gofa Province (Gidole-Chencha Horst) are mainly based on analog and numerical modeling as well as short-term geodetic observations (e.g., Stamps et al., 2008; Saria et al., 2013, 2014; Glerum et al., 2020; Philippon et al., 2014). Despite this information, the details of the structural history of many of these transfer zones has remained ambiguous, because detailed geological or paleomagnetic data do not exist to further constrain their spatiotemporal and kinematic evolution on long timescales.

Addressing this gap in knowledge, our study combines structural, geochronological, and paleomagnetic data to investigate temporally constrained deformation mechanisms during the structural linkage of rift basins. To achieve this, we chose a ~75 to 125-km-long and

~20 to 40-km-wide zone of a right-stepping rift overlap between the southern Main Ethiopian Rift and the Chew Bahir-Gofa Province in the eastern branch of the EARS for two principal reasons. First, the geochronologic constraints are excellent, and this part of the EARS is characterized by Eocene–Miocene volcanic successions (Davidson and Rex, 1980; Davidson, 1983; WoldeGabriel et al., 1991; Ebinger et al., 1993, 2000; George, 1998; George and Rogers, 2002; Bonini et al., 2005; Rooney et al., 2010) that are well-suited for additional radiometric age determination and paleomagnetic analysis of potentially rotated crustal blocks within the transfer zone. Second, extensional processes in this region have been active since ca.15 Ma (e.g., Ebinger et al., 2000; Bonini et al., 2005; Pik et al., 2008; Philippon et al., 2014; Balestrieri et al., 2016; Boone et al., 2019; Corti et al., 2019; Knappe et al., 2020; Erbello et al., 2022, 2024), and the available regional structural and stratigraphic framework allows an assessment of long-term aspects of rift-segment interaction and linkage.

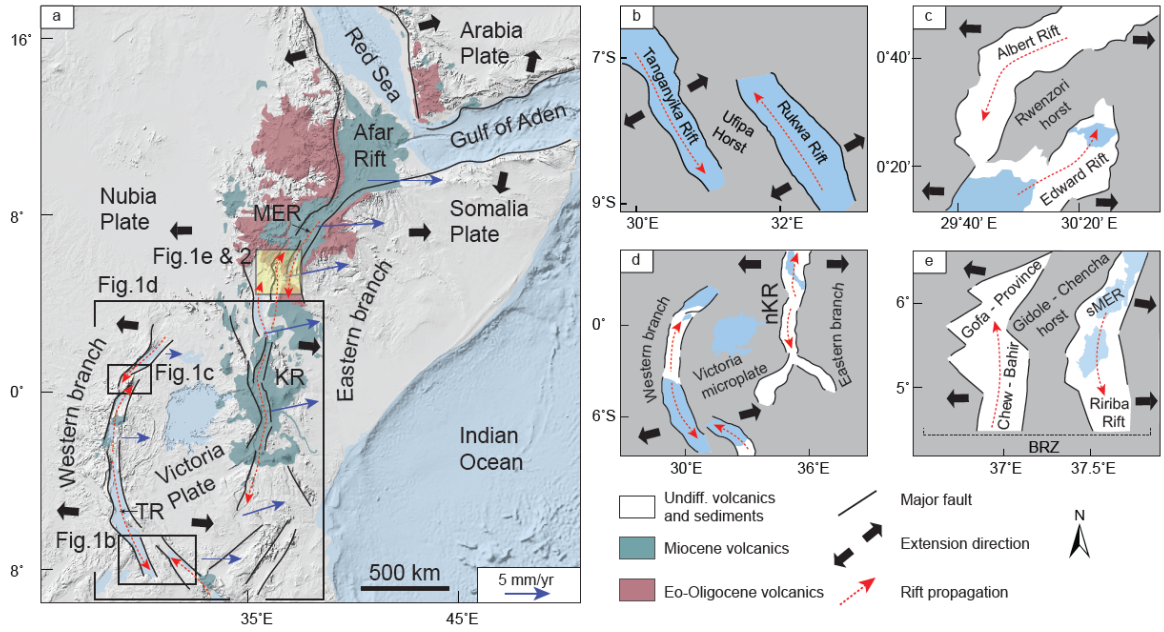

Figure 1: Tectonic setting and examples of overlapping rift segments in the East African Rift System (EARS). (a) Plate kinematics and velocity vectors (Stamps et al., 2020), principal faults, and major volcano-stratigraphic units (Rooney et al., 2017a and references therein) outcropping in the EARS (Kenya Rift, KR; Main Ethiopian Rift, MER; and Afar Rift)

153 superimposed on hill-shaded relief; (b–e) propagating (red arrow) and overlapping rift
154 segments between the Tanganyika and Rukwa rifts (b); Albert and Edward rifts (c); eastern
155 and western branches of the East African Rift System (d); and the southern Main Ethiopian
156 Rift and the Chew Bahir-Gofa Province of the study area (yellow shaded area) across the
157 Broadly Rifted Zone (BRZ) (e).
158
159 **1.1 Tectonic setting**
160 The right-stepping propagating rift segments of the southern Main Ethiopian Rift and northern
161 Kenya Rift interact across a wide region in southern Ethiopia, resulting in a structurally
162 complex extensional deformation zone with imprints of multiple tectonic events. NW-SE-
163 striking tectonic lineaments related to Cretaceous–Paleogene paleo-rifts cut obliquely NNE-
164 SSW-striking Neoproterozoic basement fabrics (Morley et al., 1992; Bosworth and Morley,
165 1994; Brune et al., 2017; Emishaw and Abdelsalam, 2019), which are sub-parallel to the N-S
166 to NE-SW-striking Cenozoic rift structures (Corti, 2009; Kendall and Lithgow-Bertelloni, 2016).
167 The Cretaceous–Paleogene lineaments are closely associated with the locations of the Melut
168 and Muglade rift basins in Sudan and South Sudan, and the Anza Rift in northern Kenya (e.g.,
169 Bosworth and Morley, 1994). Satellite gravity data from the BRZ reveals prominent, E-W-
170 striking lineaments that link the Cretaceous–Paleogene rift basins in South Sudan and
171 northern Kenya (e.g., Emishaw et al., 2019), but the structures and deposits of the N-S to NE-
172 SW-trending Cenozoic rift basins of the active EARS mostly obscure these relationships (e.g.,
173 Ebinger et al., 1993).
174 Regionally, extensional deformation related to the Nubia-Somalia plate motion appears
175 to have originated in the northern Turkana region between 35 and 25 Ma (Boone et al., 2019;
176 Ragon et al., 2019) and migrated toward the north in the Chew Bahir Basin (e.g., Bonini et al.,
177 2005 and references therein) by ~20 Ma (Pik et al., 2008). A recent low-temperature
178 thermochronology study by Erbello et al. (2024) suggests that initial diffuse faulting across the
179 BRZ likely occurred soon after the end of massive volcanism between 27 and 20 Ma. During
180 the middle to late Miocene (15 to 6 Ma), rifting had propagated farther north into the Gofa

Province, but stalled where the extensional faults intersected pre-existing NW-SE-oriented Mesozoic lineaments (Erbello et al., 2024). This suggests that strain was accommodated along these reactivated structures that strike at high angles with respect to the overall direction of rift propagation (e.g., Molnar et al., 2019).

In the study area, extensional deformation that formed the Gidole-Chencha Horst has been associated with 20 Ma N-S-striking dikes whose emplacement may have followed the reactivation of the NW-SE-oriented lineaments (Bonini et al., 2005). This contrasts the suggestion by Ebinger et al. (2000) that the main phase of faulting along the western margin of the Chamo Basin on the eastern side of the Gidole-Chencha Horst began later, at ~15 Ma. Following the development of the western margin of the Chamo Basin, faulting migrated toward the north and south of the southern Main Ethiopian Rift during the middle Miocene (e.g., Levitte, 1974; WoldeGabriel et al., 1991; Bonini et al., 2005; Boone et al., 2019). The southward migration of deformation terminated in the Ririba Rift during the late Pliocene (e.g., WoldeGabriel et al., 1991; Levitte, 1974; Ebinger et al., 2000; Bonini et al., 2005; Corti et al., 2019; Franceschini et al., 2020).

During the Quaternary, volcanism associated with extensional faulting migrated toward the present-day narrow axial zone of the southern Main Ethiopian Rift (e.g., Woldegabriel et al., 1990; Ebinger et al., 2000), along the strike of the Turkana Rift and the lower Omo Valley (Jicha and Brown, 2014). Currently, deformation is localized in the southern Gofa Province, the Chew Bahir Basin (e.g., Ebinger et al., 2000; Philippon et al., 2014; Erbello et al., 2022, 2024), and the Segen Basin (Levitte, 1974). The strain localization in these zones of overlap has been interpreted as reflecting ongoing tectonic interaction between the southern Main Ethiopian and the northern Kenya rifts (e.g., Ebinger et al., 2000; Philippon et al., 2014; Corti et al., 2019; Knappe et al., 2020; Erbello et al., 2022) via NW-SE-striking reactivated basement fabrics (Erbello et al., 2024).

In addition to focused volcano-tectonic activity across the BRZ, normal-faulting earthquakes recorded at shallow crustal depths in the region since 1913 have clustered along

208 a narrow zone between the lower Omo Valley, the southern Gofa Province, and the Chew
209 Bahir and Segen basins (Gouin, 1979; Asfaw, 1990; Ayele and Arvidsson, 1997; Foster and
210 Jackson, 1998). The limited number of earthquakes recorded a strike-slip component (Ayele,
211 and Arvidsson, 1997 2000; Bonini et al., 2005 and references therein; Musila et al., 2023,
212 Sullivan et al., 2024), supporting the notion that the current tectonic interaction between the
213 southern Main Ethiopian and the northern Kenya rifts is associated with structures striking at
214 high angle to the trend of the rift (e.g., Erbello et al., 2024).
215

216 **1.2 Geologic setting**

217 **1.2.1 Neoproterozoic basement rocks**

218 In the study area, Neoproterozoic metamorphic basement rocks comprising NNE-SSW-
219 striking foliations have been interpreted to control the site of Cenozoic rifting in the region
220 (Vauchez et al., 1997). High-grade amphibolites and layered granulites (Gichile, 1992), which
221 are characterized by NNE-SSW-striking foliations (Davidson, 1983), reflect important tectono-
222 thermal events during the collisional pan-African orogeny between 750 Ma and 550 Ma (Asrat
223 and Barbey, 2003). Structurally and temporally related basement fabrics have been mapped
224 in central-northern Kenya as well (e.g., Hetzel and Strecker, 1994), suggesting a structural
225 continuity between the two areas (Gichile, 1992), as expressed by regional structures with
226 unknown kinematics oriented sub-parallel to the Quaternary faults (e.g., Kendall and Lithgow-
227 Bertelloni, 2016). However, local E-W-striking foliations associated with layered granulites are
228 also known to occur along the southwest margin of the Chamo Basin, across the Konso
229 Plateau, and in the Segen Basin (Davidson, 1983; Gichile, 1992; Asrat and Barbey, 2003). De
230 Wit and Chewaka (1981) considered these foliations to be related to post-Pan-African tectonic
231 events associated with the emplacement of the Konso Pluton at 449 ± 2 Ma (Asrat and Barbey,
232 2003). Compositionally related plutonic rocks from the west of the Konso Plateau (Davidson,
233 1983) and the Segen Basin margin have provided radiometric ages between 526 ± 5 Ma and

554 ± 23 Ma (Gichile, 1992; Worku and Schandelmeier, 1996; Teklay et al., 1998; Yibas et al., 2002).

1.2.2 Paleogene sedimentary rocks

The volcanic units studied by us are underlain by a thin, yet prominent and silicified basal conglomeratic sandstone that unconformably covers the crystalline basement rocks (Davidson and Rex, 1980; Ebinger et al., 1993). This unit is exposed mainly along the flanks of the Amaro Horst (WoldeGabriel, 1991; Ebinger et al., 1993), where its thickness varies from 5 to 30 m along strike (WoldeGabriel, 1991; Ebinger et al., 1993); it is absent to the west of the BRZ (Moore and Davidson, 1978; Davidson, 1983; Philippon et al., 2014). Based on the sharpness of the conformable contact with overlying Eo–Oligocene volcanic rocks and the proximal sediment-clast composition, Davidson (1983) inferred an early Paleogene depositional age for this sandstone. However, Levitte et al. (1974) suggested, on the basis of petrographic characteristics, that the unit may correspond to the late Cretaceous Turkana grits of northern Kenya (Arambourg and Wolff, 1969).

1.2.3 Eocene–Oligocene volcanic rocks

The sampled Eo–Oligocene volcanic successions are well exposed along the margins of the southern Main Ethiopian Rift, the Gofa Province, and the northern Kenya Rift, with thicknesses ranging from several hundred meters to about one kilometer (Fig. 2) (Davidson, 1983; Ebinger et al., 1993, 2000; George, 1998). Across the BRZ in southern Ethiopia, these volcanic sequences document prolonged magmatism between 45 and 28 Ma (Davidson and Rex, 1980; Davidson, 1983; Ebinger et al., 2000; George and Rogers, 2002, Rooney, 2017; Steiner et al., 2021). The study area covers the Gidole-Chencha Horst between the Chew Bahir Basin-Gofa Province and the southern Main Ethiopian Rift, where volcanic eruptive centers distributed along the margin of the Chamo and Abaya basins reflect a NW-SE-oriented extension direction (Ebinger et al., 2000). The Eocene–Oligocene volcanic successions are characterized by the

Amaro basalts, the Arba-Minch tuffs, the Gamo basalts, and the Amaro tuffs (Ebinger et al., 2000; Rooney, 2017). The ~250-m-thick tholeiitic Amaro basalt is exposed along the Amaro Horst and overlies the ubiquitous Cretaceous conglomeratic sandstone layer; it constitutes the lower section of the exposed volcanic sequences and yielded a K-Ar whole-rock age of 44.9 ± 0.7 Ma (Ebinger et al., 1993). Compositionally similar basalt flows overlie the crystalline basement rocks along the southern Amaro Horst and yielded a K-Ar age of 42.5 ± 0.7 Ma (e.g., WoldeGabriel et al., 1991). The cataclastically deformed silicic Arba-Minch tuff unit, dated at ~37 and 39 Ma, is exposed along the southwestern margin of the Chamo Basin and is overlain by the 35–37 Ma Gamo basalts and the widespread Amaro tuff unit (e.g., Ebinger et al., 2000); this unit was analyzed by the Single-Crystal Laser Fusion (SCLF) dating technique, providing an age of 33 Ma (Ebinger et al., 1993, 2000).

1.2.4 Miocene volcanic rocks

The second main phase of magmatism in southern Ethiopia is documented by a sequence of early Miocene and Pliocene basalts (Levitte et al., 1974) and N-S-striking dike swarms (Bonini et al., 2005). The Oligocene Amaro tuff is generally overlain by the ~500-m-thick Getera-Kela basalt sampled in this study, which has an age range between 18 and 11 Ma (Davidson, 1983; Ebinger et al., 1993). Interbedded fluvio-lacustrine sediments within the Getera-Kela basalts that outcrop along the south-western margin of the Chamo Basin (Ebinger et al., 1993) have been biostratigraphyically dated between 17 and 15 Ma (WoldeGabriel et al., 1991). Phonolitic eruptive centers in the Segen, Mali-Dancha, and Bala-Kela basins were dated between 16 and 12 Ma; the strike of Quaternary faults follows these eruptive centers (Davidson and Rex, 1980; Ebinger et al., 2000). The Getera-Kela volcanics are capped by a basalt that provided a whole-rock K-Ar age of ~11 Ma (WoldeGabriel et al., 1991).

1.2.5 Pliocene and Quaternary volcanic rocks

After a period of volcano-tectonic quiescence during the late Miocene (e.g., Bonini et al., 2005), early Pliocene lava flows of the Gombe Group were emplaced adjacent to the Gidole-Chencha

289 Horst along the Omo-Turkana Depression (Watkins, 1986; Brown et al., 1985). Although these
290 basaltic flows were not sampled for our paleomagnetism study, they provide key markers of
291 deformation and rift evolution. A ~5-m-thick, ~4-m.y.-old basalt is exposed in the western Usno
292 Basin (Ebinger et al., 2000), extending ~150 km farther north along the Omo Valley (Davidson,
293 1983). The coeval Mursi basalts outcrop in the northern Omo Valley (Brown and Nasha, 1976).
294 In addition, outliers of petrographically similar thin basaltic flows are exposed along the
295 western margin of the Chew Bahir Basin (e.g., Davidson, 1983; Haileab et al., 2004).
296 Conventional K-Ar dating of the basaltic units within the Omo-Turkana region has revealed a
297 protracted eruptive period between ~6 and 3 Ma (e.g., Brown, 1969, Brown et al., 1985;
298 McDougall and Watkins, 1988; McDougall, 1985). More recently, Haileab et al. (2004)
299 suggested that these flows were emplaced at ~4 Ma and collectively called them Gombe
300 Group basalts (Watkins, 1983), and Erbello and Kidane (2018) further specified that these thin
301 lava flows erupted between ~4.05 and 4.18 Ma. During the late to middle Pliocene, basaltic
302 volcanism and faulting shifted eastward in the Ririba Rift (WoldeGabriel et al., 1991; Levitte,
303 1974; Ebinger et al., 2000; Bonini et al., 2005; Corti et al., 2019; Franceschini et al., 2020),
304 before magmatism became focused in a narrow zone along the Chamo Basin (e.g., Ebinger
305 et al., 1993) and Omo Valley (Jich and Brown, 2014) during the Quaternary.

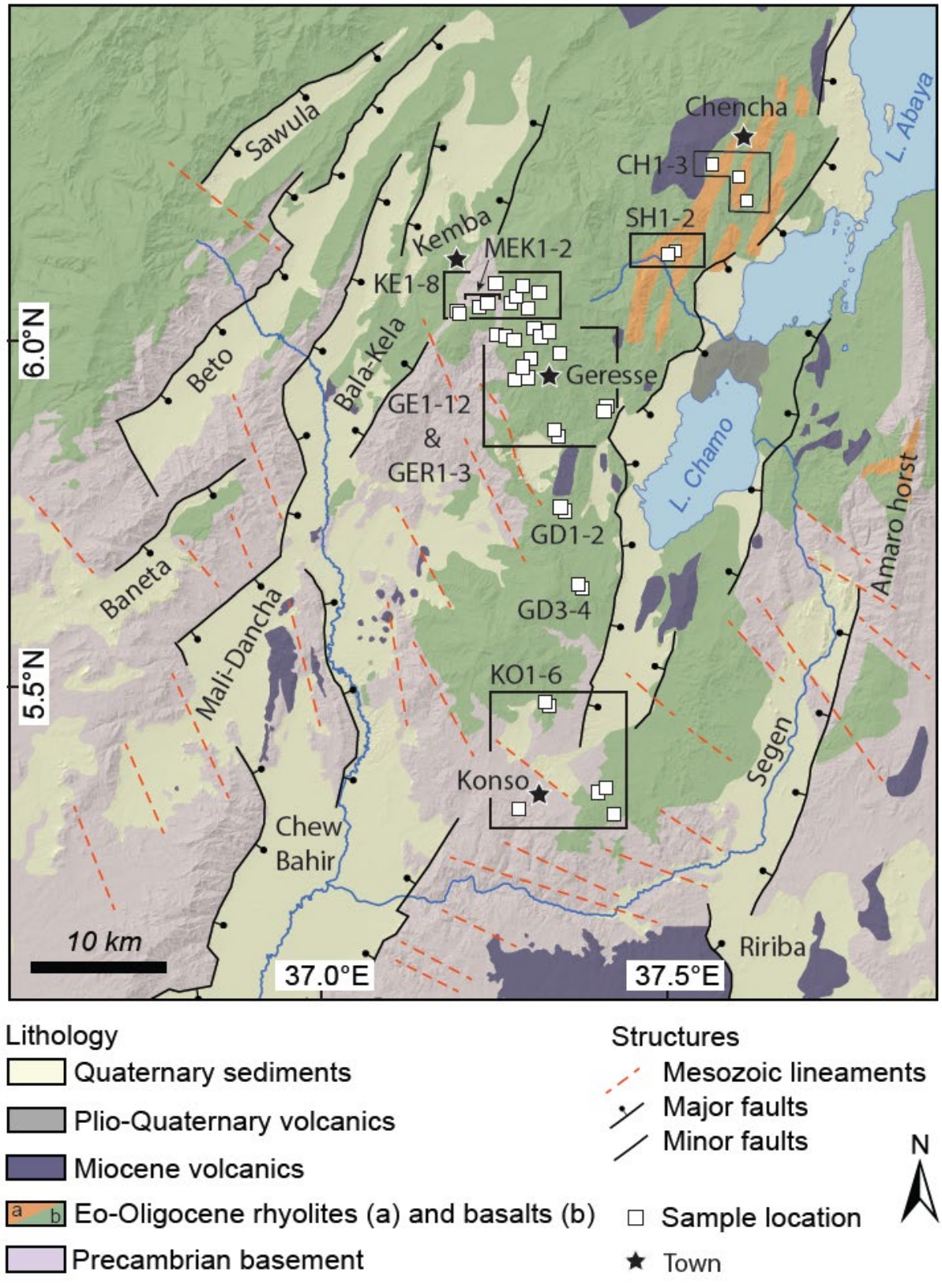

306

307 Figure 2: Geologic setting of the southern Main Ethiopian Rift and the Chew Bahir-Gofa
308 Province (Mali-Dancha, Baneta, Beto, Bala-Kela, and Sawula basins), major stratigraphic
309 units (Davidson, 1983; and Bonini et al., 2005), Mesozoic lineaments, and Quaternary faults

310 (Davidson, 1983) superimposed on hill-shaded relief. Open squares indicate sampling sites
311 grouped by locality (black boxes).
312
313 **2 Sampling and methods**

314 Volcanic and sedimentary rocks commonly archive the Earth's magnetic field during the
315 emplacement and/or deposition of the rock units (Cox, 1973; Tauxe and Kent, 1982; Butler,
316 1992; Dunlop, 1997). Subsequent tectonic movements affecting these rock units can thus be
317 reconstructed based on the paleomagnetic directions preserved in the rocks. The well-
318 exposed Eo–Oligocene and Miocene volcanics and sedimentary rocks from the Gidole-
319 Chencha Horst in southern Ethiopia are ideally suited to yield paleomagnetic signals that
320 provide information about regional tectonic deformation (Fig. 2). A total of 40 paleomagnetic
321 sites were selected from Eo–Oligocene and Miocene volcanic (37 sites) and sedimentary
322 rocks (3 sites), respectively (Table 1). Four to eight standard core samples were collected from
323 each site using a gasoline-powered motor drill. Samples were oriented using a standard
324 device with a magnetic compass and sun orientations to assess local declinations. Bedding
325 orientations were carefully measured from the top of flows and sedimentary layers for tilt
326 corrections. Additionally, eleven block samples (~1–1.5 kg) from representative sites were
327 collected for $^{40}Ar/^{39}Ar$ dating to complement the age constraints of the sampled volcanic units
328 (Table 2).

329 The paleomagnetic core samples were cut into standard specimens in sample preparation
330 laboratories at the University of Potsdam, Germany and Addis Ababa University, Ethiopia.
331 Natural remanent magnetization (NRM) of each specimen was measured before subjecting
332 the specimens to incrementally increased alternative Field (AF) and thermal (TH)
333 demagnetization experiments at the paleomagnetic laboratory of the GFZ German Research
334 Centre for Geosciences in Potsdam. About 40 of the samples were processed thermally in the
335 paleomagnetic laboratory of Addis Ababa University.

336 To define the most effective demagnetization scheme for the separation of components
337 and determination of characteristic remanent magnetizations (ChRM) to be applied in the rest
338 of the samples, pilot specimens (one per site) were first processed in AF, TH, and a
339 combination of AF and TH, with detailed demagnetization steps (5 to 120 mT for AF and 20 °C
340 to 700 °C for TH). Based on this and the rock magnetic behaviors (see 3.2.1) we ultimately
341 applied AF demagnetizations on most of the pilot specimens resulting in a well-separated
342 linear component with simple progressive decay. Based on these results, the bulk of the
343 specimens was processed by 12 AF demagnetization steps (NRM, 5, 10, 15, 20, 30, 35, 40,
344 60, 80, 100, 120 mT). ChRM directions were obtained using a principal component analysis
345 (Kirschvink, 1980) on a minimum of four consecutive steps following a procedure outlined in
346 PaleoMac 6.5 (Cogné, 2003) that was also used to determine a Fisher means of the ChRM
347 directions for each site (Fisher, 1953). To further characterize rock magnetic properties,
348 thermomagnetic experiments were performed on representative samples using a multifunction
349 kappabridge (MFK-1A) at GFZ Potsdam. Powdered samples of ~100 mg were incrementally
350 heated to 700 °C and cooled back to 40 °C while bulk magnetic susceptibility was measured
351 at a 5 °C interval.

352 To provide a temporal constraint of the sampled volcanic units, $^{40}Ar/^{39}Ar$ dating was
353 performed on representative samples at the Ar/Ar Geochronology Laboratory at the University
354 of Potsdam. The detailed Ar isotope analytical procedure is described in Wilke et al. (2010)
355 and Halama et al. (2014). A groundmass sample (~100 mg) with grain sizes ranging between
356 250 and 500 μm was prepared from fresh rock collected at eleven representative sites and
357 samples of 20 mg of each were irradiated at the Cadmium-Lined in-Core Irradiation Tube
358 facility at the Oregon State TRIGA Reactor, USA, prior to isotopic measurement at the
359 University of Potsdam. The mineral-age standard, the Fish Canyon Tuff sanidine FCs-EK
360 (Morgan et al., 2014), was irradiated together with K and Ca salts. The irradiation for all
361 samples was conducted in two phases in 2020 and 2021. The Ar isotope analyses were
362 performed by incremental heating using a 50W continuous CO_2 laser and a Micromass 5400
363 noble gas mass spectrometer. Between three consecutive step-heating experiments, a blank

364 analysis was measured for all samples. To calculate J values and unknown ages, we adopted
365 28.294 Ma for the FCs-EK sanidine, a decay constant for ^{40}K (Renne et al., 2011) and
366 atmospheric Ar composition (Lee et al., 2006). The Ar isotope analysis was carried out using
367 the “Mass Spec" software (pers. comm. A. Deino, 2020, Berkeley Geochronology Center). J
368 values and ages were calculated using a procedure described by Uto et al. (1997). Using the
369 age-spectrum displayed by measured apparent ages from each of the heating steps, a plateau
370 age was determined based on a minimum of three contiguous steps with apparent age
371 overlapping within 2σ uncertainty without the common error of the J value, and together
372 comprising >50% of the total ^{39}Ar released (Fleck et al., 1977). In order to validate the
373 estimated plateau ages, initial $^{40}Ar/^{36}Ar$ ratios obtained from normal and inverse isochrons
374 were compared, and reflect the atmospheric value (Lee et al., 2006). Subsequently, the
375 validated plateau ages were determined for each analyzed sample. In some cases when a
376 plateau was not recognized, the ages were reported as an age range (probable ages) or total
377 gas ages, following the procedure described by Schaen et al. (2020).
378
379 **3 Results**

380 **3.1 $^{40}Ar/^{39}Ar$-dating**

381 From a total of eleven analyzed samples, we finally obtained six plateau ages (Fig. 3). For the
382 remaining samples, the reported age is a total gas age or age ranges (Schaen et al., 2020).
383 The $^{40}Ar/^{39}Ar$-dating results of samples from the Gidole-Chencha Horst exhibit plateau ages
384 ranging between 42 and 38 Ma for the Gamo-Amaro basalts and between 20 and 17 Ma for
385 the Getera-Kela basalts. The details of the age determinations are provided in Table 1.
386 Sample MEK-2 collected west of the Gidole-Chencha Horst was dated at 42.441 ± 0.25
387 Ma, similar to a basaltic flow overlying crystalline basement in the southern Amaro Horst that
388 was dated at 42.53 ± 0.70 Ma (WoldeGabriel et al., 1991). Similar plateau ages of 39.44 ±
389 0.15 Ma, 39.12 ± 0.17 Ma, and 38.31 ± 0.007 Ma were obtained at sites GD-2, GE-7, and
390 MEK-1, respectively. However, a plateau age was not obtained for a sample at site CH-3; a

391 total gas age estimated from the very flat age-spectrum, occupying ~70 % fraction of the total
392 ^{39}Ar release (Fig. 3i, Table 1), records an age range between 38 and 36 Ma. Similarly, a total
393 gas age of 35.51± 0.10 Ma was obtained for a basalt sample at site KO-4 located in the south
394 of the Gidole-Chencha Horst. Sample GER-2 collected from the highly fractured welded tuff
395 unit located at a higher elevation to the west of GE-7 did not yield a plateau age, but shows a
396 relatively long flat age pattern, occupying ~80% of the total ^{39}Ar release and exhibiting an age
397 range between 35 and 32 Ma; this provided one of the probable youngest ages of all dated
398 Eo–Oligocene volcanic rocks (Fig. 3g). The welded tuff unit correlates with the widely
399 distributed Amaro tuff (~33 Ma), which separates the Eo–Oligocene rock units from ~500-m-
400 thick Miocene volcanics (Davidson, 1983; Ebinger et al., 1993; Bonini et al., 2005).
401 A pervasively fractured basalt flow exposed at site GE-1 yielded an Early Miocene plateau
402 age of 19.62 ± 0.13 Ma (Fig. 3e). Farther west across the Gidole-Chencha Horst, a basalt at
403 site GE-12, where it overlies other, sub-horizontal basalt flows (GE-10 and GE-11), was also
404 dated, but a plateau age was not obtained. Instead, the relatively long flat age pattern,
405 occupying ~65 % of the total ^{39}Ar release, corresponds to an age range between 21 and 19
406 Ma (Fig. 3h, and Table 1). These units are characterized by well-developed flow structures
407 and no intervening paleosol horizons; possibly, these basalt sheets represent laccoliths that
408 are closely linked with the N-S-striking dikes that were emplaced at about 20 Ma (e.g., Bonini
409 et al., 2005). Sample KO-1 collected from a columnar-jointed basalt located to the west of the
410 Segen basin yielded a well-constrained Miocene plateau age of 16.87 ± 0.10 Ma (Fig. 3f). Our
411 age spectra of the Miocene volcanics are compatible with the age range of the Getera-Kela
412 basalts between 18 and 11 Ma (Ebinger et al., 2000). Interestingly, our data suggest that
413 regional Miocene volcanism might have started at ~20 Ma, was closely linked with diking
414 (Bonini et al., 2005), and synchronous with faulting within the BRZ (Pik et al., 2008).

Table 1. Results of $^{40}Ar/^{39}Ar$ analyses of the Eocene and Miocene volcanic rocks from southwestern Ethiopia, East Africa.

Laser output[a]	$^{40}Ar/^{39}Ar$		$^{37}Ar/^{39}Ar$		$^{36}Ar/^{39}Ar$ (x10^{-3})		K/Ca	$^{40}Ar^*$ (%)	$^{39}Ar_K$ fraction (%)	$^{40}Ar^*/^{39}Ar_K$		Age(±1s) (Ma)	
Sample ID: CH-3 gm	*Laboratory ID: 1251*				*Irradiation ID: PO-9*								
J= (1.8729 ± 0.0026) x 10^{-3}													
1.5%	671.86	± 16.59	2.26	± 0.94	2134.35	± 56.93	0.23	5.18	0.16	34.87	± 6.94	114.38	± 22.76
1.8%	282.95	± 5.19	1.72	± 0.48	927.67	± 17.46	0.31	2.17	0.34	6.14	± 1.90	20.66	± 6.41
2.1%	272.43	± 2.60	2.34	± 0.25	854.46	± 10.27	0.22	6.43	0.77	17.53	± 2.15	58.42	± 7.16
2.4%	39.92	± 0.01	1.49	± 0.02	83.88	± 0.06	0.35	37.57	5.59	15.02	± 0.02	50.15	± 0.09
2.7%	36.77	± 0.20	1.37	± 0.10	81.17	± 0.74	0.38	34.39	8.87	12.66	± 0.24	42.37	± 0.81
3.0%	21.62	± 0.11	1.21	± 0.04	31.82	± 0.31	0.44	56.51	14.79	12.23	± 0.12	40.94	± 0.40
3.2%	12.99	± 0.03	0.94	± 0.03	6.57	± 0.08	0.56	85.49	14.07	11.11	± 0.04	37.25	± 0.13
3.4%	12.58	± 0.05	1.27	± 0.01	5.29	± 0.07	0.41	88.27	10.54	11.11	± 0.05	37.24	± 0.17
3.6%	12.49	± 0.05	1.45	± 0.05	5.12	± 0.09	0.36	88.69	8.48	11.09	± 0.06	37.16	± 0.20
3.8%	11.35	± 0.04	2.12	± 0.04	2.72	± 0.04	0.25	94.36	8.50	10.73	± 0.04	35.96	± 0.15
4.0%	11.44	± 0.05	3.20	± 0.06	2.06	± 0.08	0.16	96.88	7.49	11.11	± 0.05	37.23	± 0.19
4.2%	11.19	± 0.04	2.39	± 0.04	1.63	± 0.06	0.22	97.37	8.73	10.92	± 0.05	36.59	± 0.16
4.4%	11.29	± 0.03	5.73	± 0.05	3.49	± 0.07	0.09	94.85	11.66	10.75	± 0.04	36.05	± 0.14
	Plateau age (Ma):				no plateau				**Age range (Ma): 36-38** (steps 7-1; ^{39}Ar %:			69.5	%
	Normal isochron age (Ma) from all steps:				40.30	± 0.08			Initial $^{40}Ar/^{36}Ar$ =		331.8	± 0.3	MSWD: 22.04
	Inverse isochron age (Ma) from all steps:				36.28	± 0.08			Initial $^{40}Ar/^{36}Ar$ =		347.3	± 0.3	MSWD: 9.29
	Total gas age (Ma):				38.80	± 0.12							

Laser output[a]	$^{40}Ar/^{39}Ar$		$^{37}Ar/^{39}Ar$		$^{36}Ar/^{39}Ar$ (x10^{-3})		K/Ca	$^{40}Ar^*$ (%)	$^{39}Ar_K$ fraction (%)	$^{40}Ar^*/^{39}Ar_K$		Age(±1s) (Ma)	
Sample ID: MEK-2 gm	*Laboratory ID: 1252*				*Irradiation ID: PO-9*								
J= (1.9070 ± 0.0027) x 10^{-3}													
1.5%	4712.8	± 57.9	2.63	± 0.81	15018	± 184	0.20	4.86	0.79	229.63	± 8.79	656.69	± 25.16
1.7%	578.11	± 4.91	4.39	± 0.24	1764.2	± 16.4	0.12	8.95	2.41	51.90	± 2.26	170.66	± 7.43
1.9%	100.13	± 0.70	5.21	± 0.22	282.02	± 2.21	0.10	16.33	3.89	16.41	± 0.36	55.72	± 1.23
2.2%	38.71	± 0.25	5.71	± 0.12	83.47	± 0.79	0.09	36.82	5.18	14.31	± 0.23	48.68	± 0.80
2.5%	34.71	± 0.14	2.66	± 0.08	70.92	± 0.71	0.20	39.62	11.35	13.77	± 0.22	46.88	± 0.75
2.8%	57.23	± 0.25	1.66	± 0.06	149.13	± 0.96	0.32	22.44	18.36	12.85	± 0.27	43.79	± 0.91
3.0%	28.31	± 0.20	1.66	± 0.07	52.65	± 0.53	0.32	44.95	15.98	12.74	± 0.15	43.41	± 0.51
3.2%	27.99	± 0.08	1.58	± 0.07	51.62	± 0.63	0.33	45.39	12.05	12.72	± 0.19	43.33	± 0.66
3.5%	27.08	± 0.08	1.79	± 0.05	50.28	± 0.36	0.29	45.09	10.58	12.22	± 0.12	41.67	± 0.41
3.8%	24.53	± 0.20	4.48	± 0.14	43.05	± 0.45	0.12	49.09	6.66	12.08	± 0.19	41.18	± 0.67
4.2%	18.16	± 0.17	8.61	± 0.18	23.56	± 0.72	0.06	65.09	4.58	11.89	± 0.25	40.54	± 0.84
4.4%	23.53	± 0.27	12.54	± 0.33	42.58	± 1.15	0.04	50.28	3.23	11.93	± 0.38	40.68	± 1.28
4.9%	38.76	± 0.30	13.19	± 0.32	84.00	± 0.89	0.04	38.04	4.93	14.88	± 0.25	50.58	± 0.86
	Plateau age (Ma):				**42.44**	± **0.25**			Plateau steps:	6th to 10th	^{39}Ar %:	63.6	%
	Normal isochron age (Ma) from plateau:				41.28	± 0.59			Initial $^{40}Ar/^{36}Ar$ =		304.0	± 2.8	MSWD: 1.97
	Inverse isochron age (Ma) from plateau:				41.33	± 0.59			Initial $^{40}Ar/^{36}Ar$ =		303.9	± 2.8	MSWD: 1.98
	Total gas age (Ma):				53.24	± 0.38							

Laser output[a]	$^{40}Ar/^{39}Ar$		$^{37}Ar/^{39}Ar$		$^{36}Ar/^{39}Ar$ (x10^{-3})		K/Ca	$^{40}Ar^*$ (%)	$^{39}Ar_K$ fraction (%)	$^{40}Ar^*/^{39}Ar_K$		Age(±1s) (Ma)	
Sample ID: KE-1 gm	*Laboratory ID: 1253*				*Irradiation ID: PO-9*								
J= (1.9007 ± 0.0026) x 10^{-3}													
1.5%	92.91	± 0.76	1.34	± 0.26	264.88	± 2.52	0.39	15.00	0.97	13.95	± 0.46	47.30	± 1.55
1.8%	28.41	± 0.12	1.80	± 0.08	56.60	± 0.4	0.29	41.02	3.92	11.67	± 0.12	39.7	± 0.4
2.0%	39.56	± 0.12	2.18	± 0.06	88.08	± 0.4	0.24	33.98	5.39	13.46	± 0.12	45.7	± 0.4
2.4%	34.79	± 0.09	2.06	± 0.05	68.51	± 0.3	0.26	41.68	9.60	14.52	± 0.09	49.2	± 0.3
2.6%	30.63	± 0.07	1.72	± 0.04	56.47	± 0.2	0.30	45.42	12.29	13.93	± 0.07	47.2	± 0.2
2.8%	25.70	± 0.07	1.65	± 0.02	42.88	± 0.3	0.32	50.71	13.88	13.05	± 0.10	44.3	± 0.3
3.0%	22.87	± 0.08	1.60	± 0.01	33.79	± 0.12	0.33	56.44	12.47	12.92	± 0.06	43.9	± 0.2
3.2%	21.90	± 0.07	1.70	± 0.04	31.82	± 0.2	0.31	57.25	10.22	12.55	± 0.08	42.6	± 0.3
3.4%	22.39	± 0.08	1.64	± 0.14	32.82	± 0.3	0.32	56.83	7.79	12.74	± 0.10	43.3	± 0.3

415

3.7%	22.13	±	0.08	2.26	±	0.05	29.14	±	0.2	0.23	61.51	8.51	13.63	±	0.08	46.3	± 0.3
4.1%	24.04	±	0.10	3.22	±	0.06	39.88	±	0.3	0.16	51.56	7.58	12.42	±	0.10	42.2	± 0.3
4.4%	23.77	±	0.08	5.30	±	0.08	40.08	±	0.3	0.10	51.46	7.38	12.28	±	0.11	41.7	± 0.4

Plateau age (Ma): no plateau

Normal isochron age (Ma) from all steps: 41.93 ± 0.23 Initial $^{40}Ar/^{36}Ar$ = 314.7 ± 1.3 MSWD: 7.83

Inverse isochron age (Ma) from all steps: 42.00 ± 0.22 Initial $^{40}Ar/^{36}Ar$ = 315.7 ± 1.3 MSWD: 7.74

Total gas age (Ma): 44.47 ± 0.09

Laser output#	$^{40}Ar/^{39}Ar$		$^{37}Ar/^{39}Ar$		$^{36}Ar/^{39}Ar$ (x10^{-3})		K/Ca	$^{40}Ar^*$ (%)	$^{39}Ar_K$ fraction (%)	$^{40}Ar^*/^{39}Ar_K$		Age(±1s) (Ma)	
Sample ID: GER-3 gm					*Laboratory ID: 1254*			*Irradiation ID: PO-9*					
J= (1.8887 ± 0.0026) x 10^{-3}													
1.5%	390.62	± 2.41	1.05	± 0.12	1205.7	± 8.5	0.50	7.87	2.93	30.75	± 1.36	102.07	± 4.53
1.8%	156.67	± 0.57	2.13	± 0.07	443.5	± 2.3	0.25	15.60	5.75	24.47	± 0.57	81.69	± 1.89
2.1%	39.86	± 0.19	5.89	± 0.13	83.52	± 0.79	0.09	38.62	5.09	15.45	± 0.24	52.02	± 0.80
2.4%	24.61	± 0.14	8.75	± 0.10	49.49	± 0.46	0.06	42.82	5.69	10.60	± 0.17	35.84	± 0.57
2.7%	20.40	± 0.09	5.76	± 0.10	37.04	± 0.25	0.09	48.07	9.60	9.84	± 0.08	33.30	± 0.28
2.9%	29.64	± 0.11	7.72	± 0.12	69.05	± 0.35	0.07	32.55	7.30	9.70	± 0.09	32.82	± 0.32
3.1%	21.97	± 0.09	6.29	± 0.11	42.32	± 0.26	0.08	44.81	8.64	9.89	± 0.09	33.46	± 0.30
3.3%	18.34	± 0.08	8.84	± 0.25	32.00	± 0.25	0.06	51.80	6.89	9.56	± 0.09	32.35	± 0.31
3.5%	17.22	± 0.10	9.07	± 0.14	27.43	± 0.55	0.06	56.69	6.57	9.82	± 0.18	33.23	± 0.60
3.7%	15.35	± 0.05	6.28	± 0.12	20.09	± 0.16	0.08	64.21	9.87	9.90	± 0.06	33.48	± 0.22
3.9%	18.42	± 0.06	6.28	± 0.07	30.16	± 0.22	0.08	53.87	8.68	9.96	± 0.08	33.71	± 0.26
4.1%	18.42	± 0.06	6.28	± 0.07	30.16	± 0.22	0.08	53.87	8.68	9.96	± 0.08	33.71	± 0.26
4.4%	21.58	± 0.12	6.12	± 0.12	39.93	± 0.57	0.09	47.03	6.88	10.19	± 0.17	34.47	± 0.59
4.7%	11.53	± 0.08	4.18	± 0.08	7.42	± 0.12	0.13	83.71	7.43	9.68	± 0.08	32.74	± 0.27

Plateau age (Ma): no plateau **Age range (Ma): 32-35** (steps 5-1:^{39}Ar %: 80.5 %

Normal isochron age (Ma) from all steps: 31.17 ± 0.14 Initial $^{40}Ar/^{36}Ar$ = 320.7 ± 0.8 MSWD: 6.53

Inverse isochron age (Ma) from all steps: 31.14 ± 0.13 Initial $^{40}Ar/^{36}Ar$ = 322.5 ± 0.8 MSWD: 7.00

Total gas age (Ma): 39.21 ± 0.20

Laser output#	$^{40}Ar/^{39}Ar$		$^{37}Ar/^{39}Ar$		$^{36}Ar/^{39}Ar$ (x10^{-3})		K/Ca	$^{40}Ar^*$ (%)	$^{39}Ar_K$ fraction (%)	$^{40}Ar^*/^{39}Ar_K$		Age(±1s) (Ma)	
Sample ID: GE-13 gm					*Laboratory ID: 1256*			*Irradiation ID: PO-9*					
J= (1.8887 ± 0.0026) x 10^{-3}													
1.5%	1369.4	± 7.2	0.000	± 0.139	4582.1	± 25.1	7363	0.10	0.52	1.41	± 2.24	4.79	± 7.63
1.7%	558.2	± 162.7	0.015	± 0.043	1808.8	± 527.2	36	3.26	1.14	18.18	± 5.51	60.89	± 18.45
1.9%	80.66	± 0.32	0.005	± 0.009	242.5	± 1.0	112	10.24	7.12	8.26	± 0.17	27.91	± 0.57
2.1%	28.88	± 0.07	0.002	± 0.005	73.00	± 0.41	212	24.53	13.47	7.08	± 0.11	23.96	± 0.39
2.3%	18.26	± 0.05	0.001	± 0.005	38.17	± 0.68	526	37.58	11.39	6.86	± 0.20	23.22	± 0.68
2.5%	14.83	± 0.05	0.000	± 0.004	28.89	± 0.19	119807	41.84	8.46	6.20	± 0.06	21.01	± 0.19
2.7%	13.08	± 0.04	0.005	± 0.007	23.07	± 0.11	103	47.34	6.42	6.19	± 0.03	20.97	± 0.12
2.9%	11.19	± 0.05	0.000	± 0.007	16.70	± 0.12	82556	55.44	5.84	6.20	± 0.04	21.01	± 0.14
3.1%	9.58	± 0.03	0.006	± 0.008	12.09	± 0.13	91	62.34	6.24	5.97	± 0.04	20.23	± 0.15
3.3%	8.64	± 0.03	0.000	± 0.006	9.17	± 0.13	1865	68.32	6.79	5.91	± 0.04	20.00	± 0.15
3.5%	8.17	± 0.03	0.005	± 0.006	8.04	± 0.09	98	70.66	7.38	5.78	± 0.03	19.57	± 0.12
3.7%	7.91	± 0.03	0.008	± 0.006	6.82	± 0.05	65	74.25	9.07	5.87	± 0.03	19.88	± 0.10
3.9%	8.20	± 0.03	0.015	± 0.006	7.73	± 0.23	36	71.87	8.45	5.89	± 0.07	19.96	± 0.25
4.1%	9.60	± 0.05	0.013	± 0.009	12.38	± 0.11	40	61.51	4.30	5.91	± 0.04	20.00	± 0.14
4.3%	12.97	± 0.04	0.000	± 0.016	23.83	± 0.32	32241	45.14	2.31	5.85	± 0.10	19.83	± 0.33
4.5%	19.83	± 0.08	0.080	± 0.041	42.94	± 1.01	7	35.38	1.10	7.01	± 0.30	23.74	± 1.02

Plateau age (Ma): no plateau **Age range (Ma): 19-21** (steps 6-1:^{39}Ar %: 65.3 %

Normal isochron age (Ma) from all steps: 20.07 ± 0.06 Initial $^{40}Ar/^{36}Ar$ = 302.6 ± 0.4 MSWD: 4.99

Inverse isochron age (Ma) from all steps: 20.09 ± 0.06 Initial $^{40}Ar/^{36}Ar$ = 302.8 ± 0.4 MSWD: 5.01

Total gas age (Ma): 22.02 ± 0.15

Laser output#	$^{40}Ar/^{39}Ar$	$^{37}Ar/^{39}Ar$	$^{36}Ar/^{39}Ar$ (x10^{-3})	K/Ca	$^{40}Ar^*$ (%)	$^{39}Ar_K$ fraction (%)	$^{40}Ar^*/^{39}Ar_K$	Age(±1s) (Ma)

416

Sample ID: MEK-1 hf *Laboratory ID: 1257* *Irradiation ID: PO-9*

J= (1.9041 ± 0.0026) x 10^{-3}

Laser output	$^{40}Ar/^{39}Ar$	±	$^{37}Ar/^{39}Ar$	±	$^{36}Ar/^{39}Ar$ (x10^{-3})	±	K/Ca	$^{40}Ar^{*}$ (%)	$^{39}Ar_K$ fraction (%)	$^{40}Ar^{*}/^{39}Ar_K$	±	Age(±1s) (Ma)	±
1.6%	43.98	1.20	0.001	0.773	105.76	3.69	755	28.20	0.25	12.40	0.78	42.20	2.66
2.0%	12.25	0.09	0.00	0.11	0.98	0.23	5196	97.60	1.71	11.96	0.11	40.71	0.38
2.2%	11.61	0.09	0.00	0.11	1.07	0.23	5352	97.26	1.76	11.29	0.12	38.47	0.40
2.4%	11.47	0.08	0.00	0.09	0.81	0.16	7026	97.89	2.32	11.22	0.09	38.24	0.32
2.6%	11.38	0.07	0.00	0.06	0.79	0.10	10192	97.92	3.37	11.14	0.08	37.97	0.27
2.8%	11.36	0.06	0.02	0.04	0.83	0.07	31	97.83	6.25	11.11	0.06	37.85	0.21
2.9%	11.39	0.04	0.00	0.02	0.19	0.04	232	99.52	9.34	11.33	0.04	38.60	0.14
3.0%	11.27	0.03	0.07	0.02	0.33	0.03	7	99.18	12.07	11.18	0.03	38.07	0.12
3.1%	11.21	0.03	0.00	0.02	0.03	0.04	301	99.92	10.21	11.20	0.03	38.15	0.12
3.2%	11.40	0.05	0.02	0.05	0.11	0.11	33	99.72	3.73	11.37	0.06	38.73	0.22
3.4%	11.30	0.08	0.04	0.06	0.41	0.14	14	98.96	3.06	11.19	0.09	38.11	0.30
3.7%	11.27	0.07	0.00	0.05	0.20	0.11	10918	99.46	3.62	11.21	0.08	38.18	0.26
4.0%	11.20	0.05	0.00	0.04	0.00	0.09	12495	100.00	4.15	11.20	0.06	38.14	0.20
4.3%	11.30	0.04	0.000	0.013	0.12	0.02	44741	99.67	14.86	11.26	0.04	38.35	0.16
4.6%	11.34	0.05	0.014	0.008	0.10	0.02	37	99.75	23.31	11.31	0.05	38.53	0.17

Plateau age (Ma): **38.31** ± **0.07** Plateau steps: 9th to 15th ^{39}Ar %: 62.9 %

Normal isochron age (Ma) from plateau: 38.23 ± 0.15 Initial $^{40}Ar/^{36}Ar$ = 246.7 ± 250.4 MSWD: 0.88

Inverse isochron age (Ma) from plateau: 38.04 ± 0.15 Initial $^{40}Ar/^{36}Ar$ = 970.9 ± 404.0 MSWD: 1.12

Total gas age (Ma): 38.27 ± 0.06

Sample ID: GE-7 gm *Laboratory ID: 1290* *Irradiation ID: PO-10*

J= (1.8822 ± 0.0043) x 10^{-3}

Laser output	$^{40}Ar/^{39}Ar$	±	$^{37}Ar/^{39}Ar$	±	$^{36}Ar/^{39}Ar$ (x10^{-3})	±	K/Ca	$^{40}Ar^{*}$ (%)	$^{39}Ar_K$ fraction (%)	$^{40}Ar^{*}/^{39}Ar_K$	±	Age(±1s) (Ma)	±
1.4%	242.93	4.05	1.78	0.70	787.60	13.94	0.30	3.26	0.63	7.93	1.79	26.80	6.06
1.7%	45.24	0.47	2.62	0.22	108.42	1.30	0.20	28.92	2.92	13.11	0.33	44.08	1.10
2.2%	17.78	0.19	2.22	0.13	19.14	0.37	0.24	68.88	5.32	12.26	0.17	41.26	0.59
2.4%	14.60	0.12	1.81	0.09	10.43	0.17	0.29	79.68	11.03	11.65	0.12	39.21	0.40
2.6%	14.42	0.08	1.37	0.07	9.69	0.13	0.38	80.71	14.34	11.65	0.09	39.23	0.30
2.8%	15.85	0.14	1.12	0.11	14.50	0.18	0.47	73.26	12.53	11.62	0.12	39.14	0.42
3.0%	16.99	0.13	1.41	0.10	17.77	0.25	0.37	69.44	9.27	11.81	0.13	39.74	0.44
3.2%	16.89	0.15	1.45	0.14	18.68	0.24	0.36	67.69	8.69	11.44	0.14	38.54	0.47
3.5%	18.86	0.20	2.22	0.12	25.70	0.34	0.24	60.29	8.49	11.39	0.17	38.36	0.58
3.8%	18.38	0.10	6.51	0.10	27.60	0.25	0.08	58.06	12.48	10.72	0.10	36.12	0.34
4.1%	18.29	0.12	11.86	0.20	27.07	0.26	0.04	61.11	14.28	11.27	0.12	37.96	0.42

Plateau age (Ma): **39.12** ± **0.17** Plateau steps: 4th to 9th ^{39}Ar %: 64.4 %

Normal isochron age (Ma) from plateau: 39.56 ± 0.49 Initial $^{40}Ar/^{36}Ar$ = 287.1 ± 9.9 MSWD: 1.04

Inverse isochron age (Ma) from plateau: 39.55 ± 0.49 Initial $^{40}Ar/^{36}Ar$ = 287.5 ± 9.9 MSWD: 1.06

Total gas age (Ma): 38.65 ± 0.14

Sample ID: GE-1 gm *Laboratory ID: 1291* *Irradiation ID: PO-10*

J= (1.8789 ± 0.0043) x 10^{-3}

Laser output	$^{40}Ar/^{39}Ar$	±	$^{37}Ar/^{39}Ar$	±	$^{36}Ar/^{39}Ar$ (x10^{-3})	±	K/Ca	$^{40}Ar^{*}$ (%)	$^{39}Ar_K$ fraction (%)	$^{40}Ar^{*}/^{39}Ar_K$	±	Age(±1s) (Ma)	±
1.4%	1006.5	13.0	10.41	2.61	3360.6	54.5	0.05	0.40	0.16	4.03	11.68	13.64	39.53
1.7%	190.96	3.44	5.87	0.91	593.5	12.8	0.09	7.45	0.53	14.29	2.85	47.90	9.54
2.0%	70.99	1.24	3.75	0.53	221.50	5.59	0.14	7.27	0.97	5.18	1.34	17.50	4.52
2.2%	31.29	0.48	4.27	0.25	83.23	2.02	0.12	21.70	1.96	6.81	0.58	22.99	1.98
2.4%	20.56	0.19	2.81	0.15	50.81	1.03	0.19	27.33	3.85	5.63	0.30	19.03	1.03
2.6%	16.26	0.11	2.34	0.11	33.73	0.26	0.22	39.24	8.88	6.39	0.11	21.58	0.38
2.8%	11.06	0.09	1.67	0.06	16.66	0.15	0.31	56.27	22.63	6.23	0.07	21.05	0.23
3.0%	7.07	0.05	1.28	0.04	4.64	0.05	0.41	81.87	32.06	5.79	0.05	19.56	0.17
3.2%	7.45	0.05	1.22	0.06	5.63	0.20	0.43	78.77	13.29	5.87	0.07	19.85	0.26
3.5%	10.25	0.08	3.35	0.14	16.32	0.49	0.16	55.13	6.31	5.67	0.16	19.15	0.55
3.8%	11.73	0.14	9.17	0.25	22.54	0.66	0.06	49.00	3.87	5.79	0.23	19.55	0.79
4.3%	11.11	0.09	10.70	0.28	20.71	0.58	0.05	52.21	5.48	5.85	0.19	19.75	0.64

Plateau age (Ma): **19.62** ± **0.13** Plateau steps: 8th to 12th ^{39}Ar %: 61.0 %

417

	Normal isochron age (Ma) from plateau:	19.64	±	0.23		Initial $^{40}Ar/^{36}Ar$ =	295.4	±	8.9	MSWD:	0.74						
	Inverse isochron age (Ma) from plateau:	19.64	±	0.23		Initial $^{40}Ar/^{36}Ar$ =	295.6	±	8.9	MSWD:	0.74						
	Total gas age (Ma):	20.22	±	0.15													

Laser output[#]	$^{40}Ar/^{39}Ar$		$^{37}Ar/^{39}Ar$		$^{36}Ar/^{39}Ar$ (x10^{-3})		K/Ca	$^{40}Ar^{*}$ (%)	$^{39}Ar_K$ fraction (%)	$^{40}Ar^{*}/^{39}Ar_K$			Age(±1s) (Ma)	
Sample ID: GD-3 gm	*Laboratory ID: 1292*				*Irradiation ID: PO-10*									
J=	*(1.8677 ± 0.0043) x 10^{-3}*													
1.4%	1679.7	± 42.1	6.98	± 6.24	5593.8	± 149.1	0.08	0.60	0.09	10.20	± 19.75	34.12	±	66.07
1.7%	351.56	± 9.40	5.80	± 1.40	1145.1	± 32.8	0.09	2.88	0.37	10.18	± 5.11	34.06	±	17.09
2.0%	117.72	± 2.31	4.22	± 0.89	379.77	± 9.49	0.12	3.98	0.65	4.70	± 2.46	15.79	±	8.28
2.2%	56.28	± 0.90	3.57	± 0.43	145.86	± 3.58	0.15	23.14	1.28	13.05	± 1.00	43.55	±	3.34
2.4%	19.25	± 0.21	1.74	± 0.13	23.21	± 0.84	0.30	64.74	3.18	12.48	± 0.29	41.65	±	0.99
2.6%	15.48	± 0.12	1.23	± 0.10	11.23	± 0.20	0.43	78.99	5.20	12.24	± 0.12	40.86	±	0.42
2.8%	12.61	± 0.09	1.22	± 0.03	3.54	± 0.06	0.43	92.41	23.52	11.66	± 0.09	38.96	±	0.30
3.0%	12.47	± 0.06	1.29	± 0.05	2.61	± 0.10	0.41	94.59	24.25	11.81	± 0.07	39.44	±	0.25
3.2%	12.36	± 0.06	1.30	± 0.06	1.97	± 0.07	0.40	96.09	14.01	11.89	± 0.06	39.71	±	0.23
3.5%	12.13	± 0.08	2.55	± 0.09	2.63	± 0.08	0.21	95.23	11.33	11.57	± 0.08	38.67	±	0.29
3.9%	11.98	± 0.10	3.74	± 0.09	2.74	± 0.06	0.14	95.71	16.12	11.49	± 0.10	38.41	±	0.34
	Plateau age (Ma):				**39.44**	± **0.15**		Plateau steps:	7th to 9th	^{39}Ar %:	61.8	%		
	Normal isochron age (Ma) from plateau:	39.84	±	0.52		Initial $^{40}Ar/^{36}Ar$ =	227.4	±	67.6	MSWD:	1.10			
	Inverse isochron age (Ma) from plateau:	40.39	±	0.51		Initial $^{40}Ar/^{36}Ar$ =	156.1	±	67.3	MSWD:	0.11			
	Total gas age (Ma):	39.04	±	0.16										

Laser output[#]	$^{40}Ar/^{39}Ar$		$^{37}Ar/^{39}Ar$		$^{36}Ar/^{39}Ar$ (x10^{-3})		K/Ca	$^{40}Ar^{*}$ (%)	$^{39}Ar_K$ fraction (%)	$^{40}Ar^{*}/^{39}Ar_K$			Age(±1s) (Ma)	
Sample ID: EO-1 gm	*Laboratory ID: 1293*				*Irradiation ID: PO-10*									
J=	*(1.8701 ± 0.0043) x 10^{-3}*													
1.4%	428.90	± 4.18	0.00	± 0.72	1379.3	± 14.1	487.59	3.98	0.55	17.08	± 2.62	56.87	±	8.71
1.7%	100.07	± 1.27	1.19	± 0.33	297.50	± 3.87	0.44	11.34	1.66	11.36	± 0.71	38.01	±	2.37
2.0%	66.16	± 0.51	1.20	± 0.16	199.69	± 1.63	0.44	10.03	4.09	6.64	± 0.34	22.33	±	1.13
2.2%	27.67	± 0.25	1.39	± 0.13	75.88	± 0.71	0.38	18.52	5.62	5.13	± 0.22	17.26	±	0.74
2.4%	18.77	± 0.13	1.01	± 0.08	45.54	± 0.36	0.52	28.01	9.53	5.26	± 0.12	17.71	±	0.41
2.6%	13.26	± 0.07	1.19	± 0.08	27.82	± 0.18	0.44	38.07	15.69	5.05	± 0.08	17.00	±	0.28
2.8%	9.75	± 0.07	1.17	± 0.06	16.36	± 0.14	0.45	50.88	16.64	4.96	± 0.07	16.71	±	0.24
3.0%	8.31	± 0.04	1.13	± 0.07	11.61	± 0.12	0.47	59.37	14.49	4.94	± 0.05	16.61	±	0.18
3.2%	7.26	± 0.05	1.79	± 0.13	7.90	± 0.14	0.29	69.52	9.75	5.06	± 0.06	17.02	±	0.21
3.5%	10.37	± 0.07	2.52	± 0.14	17.97	± 0.23	0.21	50.26	7.70	5.22	± 0.09	17.57	±	0.31
3.9%	6.97	± 0.04	5.19	± 0.16	9.19	± 0.12	0.10	66.70	14.29	4.66	± 0.05	15.70	±	0.19
	Plateau age (Ma):				**16.87**	± **0.10**		Plateau steps:	4th to 9th	^{39}Ar %:	71.7	%		
	Normal isochron age (Ma) from plateau:	16.58	±	0.17		Initial $^{40}Ar/^{36}Ar$ =	302.8	±	2.4	MSWD:	1.09			
	Inverse isochron age (Ma) from plateau:	16.60	±	0.17		Initial $^{40}Ar/^{36}Ar$ =	302.7	±	2.4	MSWD:	1.10			
	Total gas age (Ma):	17.59	±	0.12										

Laser output[#]	$^{40}Ar/^{39}Ar$		$^{37}Ar/^{39}Ar$		$^{36}Ar/^{39}Ar$ (x10^{-3})		K/Ca	$^{40}Ar^{*}$ (%)	$^{39}Ar_K$ fraction (%)	$^{40}Ar^{*}/^{39}Ar_K$			Age(±1s) (Ma)	
Sample ID: EO-4 gm	*Laboratory ID: 1294*				*Irradiation ID: PO-10*									
J=	*(1.8729 ± 0.0043) x 10^{-3}*													
1.4%	63.60	± 0.69	0.66	± 0.20	187.77	± 2.02	0.80	11.94	1.34	7.60	± 0.55	25.56	±	1.84
1.7%	17.86	± 0.09	0.38	± 0.03	24.16	± 0.19	1.39	59.79	10.41	10.68	± 0.08	35.83	±	0.29
2.0%	14.09	± 0.09	0.68	± 0.03	9.09	± 0.09	0.77	81.13	18.12	11.43	± 0.08	38.31	±	0.29
2.2%	13.13	± 0.08	1.10	± 0.05	6.47	± 0.09	0.48	85.97	9.13	11.30	± 0.08	37.87	±	0.28
2.4%	12.47	± 0.08	1.15	± 0.08	5.21	± 0.11	0.46	88.27	6.84	11.02	± 0.08	36.94	±	0.28
2.6%	12.26	± 0.10	1.22	± 0.09	5.09	± 0.13	0.43	88.41	5.19	10.85	± 0.11	36.36	±	0.36
2.9%	11.40	± 0.08	1.63	± 0.11	4.74	± 0.14	0.32	88.74	4.90	10.12	± 0.09	33.96	±	0.31
3.2%	12.01	± 0.10	1.37	± 0.12	6.39	± 0.11	0.38	85.06	7.91	10.23	± 0.10	34.31	±	0.33
3.5%	11.75	± 0.06	2.12	± 0.07	5.65	± 0.08	0.25	87.12	12.23	10.25	± 0.06	34.38	±	0.23
3.8%	11.41	± 0.08	4.10	± 0.12	5.58	± 0.07	0.13	88.32	17.95	10.11	± 0.07	33.91	±	0.26
4.1%	10.78	± 0.09	9.62	± 0.39	5.13	± 0.14	0.05	93.06	4.64	10.10	± 0.11	33.88	±	0.37

418

4.4%	11.09	± 0.18	13.38	± 0.67	6.29	± 0.42	0.04	92.89	1.34	10.39	± 0.22	34.86	±	0.75			
	Plateau age (Ma):				no plateau												
	Normal isochron age (Ma) from plateau:	35.40	±	0.13		Initial $^{40}Ar/^{36}Ar$ =	295.5	±	2.5	MSWD:	6.26						
	Inverse isochron age (Ma) from plateau:	35.80	±	0.14		Initial $^{40}Ar/^{36}Ar$ =	293.3	±	2.5	MSWD:	6.26						
	Total gas age (Ma):	**35.51**	±	**0.10**													

[#]100% corresponds to 50W output of CO_2 laser. All the errors indicate 1 sigma error. $^{40}Ar^{*}$ means radiogenic ^{40}Ar.

419

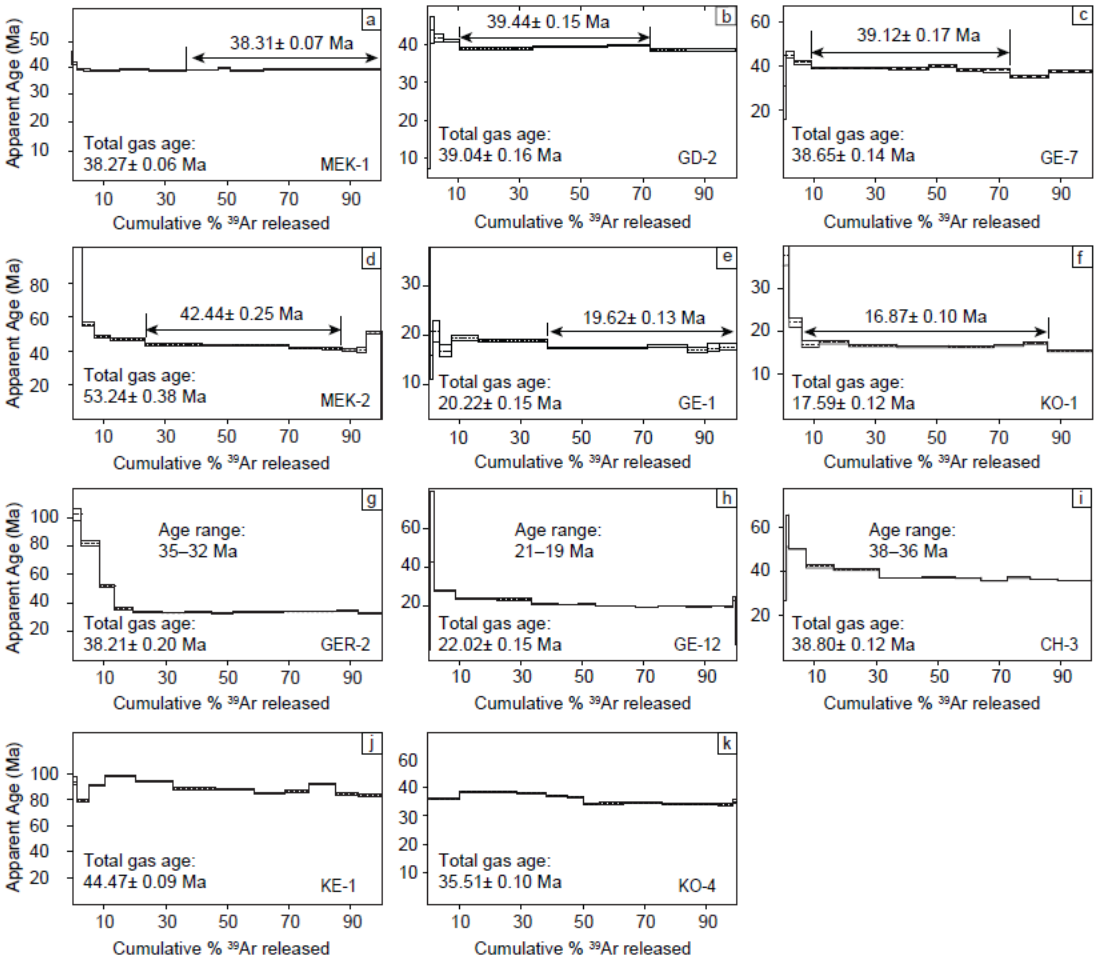

Figure 3: Representative $^{40}Ar/^{39}Ar$-dating results from basaltic flows sampled for paleomagnetic analyses across the Gidole-Chencha Horst. (a–f) Plateau ages obtained for samples from consecutive heating experiments; (g–i) age range for the samples estimated from relatively long flat age patterns (Schaen et al., 2020), occupying >65% of the fraction of ^{39}Ar release. The total gas age is shown for all samples.

3.2 Paleomagnetic results

Based on our new $^{40}Ar/^{39}Ar$ data presented above, existing regional geochronologic information (e.g., Davidson and Rex, 1980; Davidson, 1983; Ebinger et al., 1993, 2000; George, 1998; George and Rogers, 2002; Bonini et al., 2005; Rooney et al., 2010), as well as detailed petrographic studies (e.g., Steiner et al., 2021), we gathered the sampled paleomagnetic sites into an Eo–Oligocene age group (45–27 Ma; e.g., Steiner et al., 2021)

433 and a Miocene age group (20–11 Ma). We also established a relative stratigraphic section for
434 the sampled units (Fig. 4).

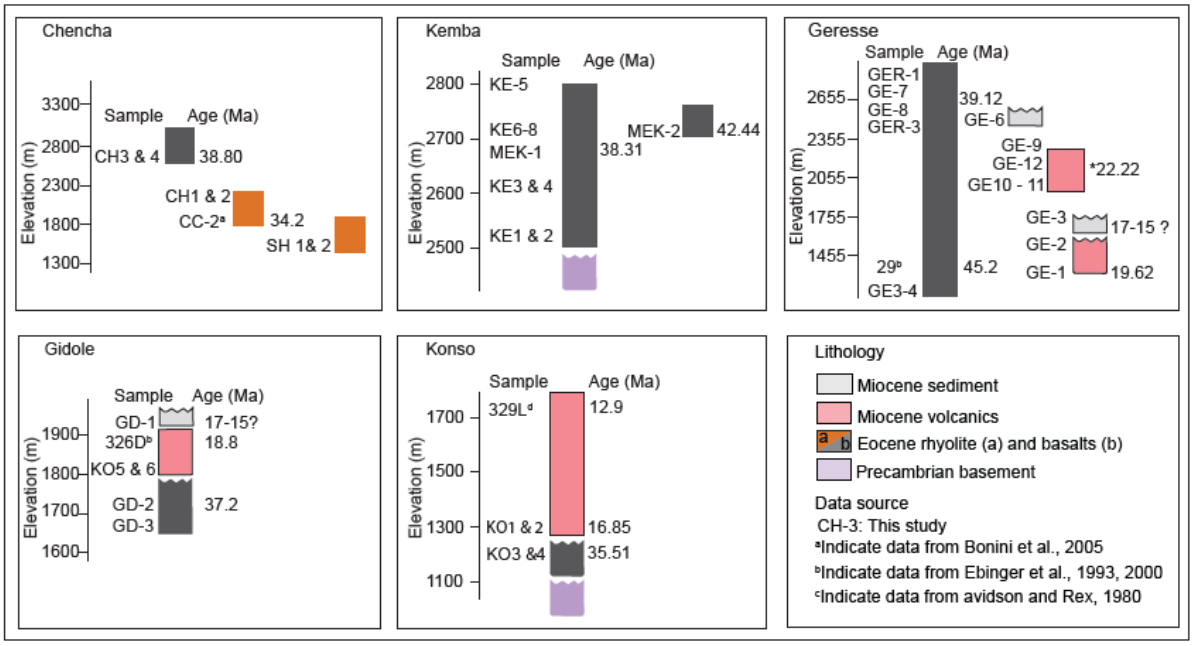

435

436 Figure 4: Chronostratigraphic sections for the sampled Chencha, Kemba, Geresse, Gidole
437 and Konso localities. Geochronologic results from our study and regional age information were
438 combined with specific sampling locations for each site and used to establish a relative
439 stratigraphy.

440

441 **3.2.1 Rock magnetic behavior**

442 The NRM intensities measured prior to the demagnetization experiments provided an average
443 value of 1.1 and 7.1 A/m for the Eo–Oligocene and Miocene rocks, respectively (Fig. 5). The
444 thermal demagnetizations of pilot samples showed limited decay between 0 and 150 °C
445 suggesting goethite does not significantly contribute to the magnetization (Dunlop and
446 Ozdemir, 2007; Figs. 6 and 7). Further thermal decay of demagnetizations showed simple
447 univectorial decay of most of the NRM between 400 and 600 °C typical of volcanic rocks with
448 strong magnetizations dominated by titanomagnetite. Only about four of the pilot samples
449 (Figs. 6b, f and 7d) exhibit a final decay between 600 and 680 °C, suggesting the presence of
450 hematite or its formation during thermal demagnetization. Comparison with thermomagnetic

451 runs and AF demagnetizations provide further insight. Thermomagnetic runs (Fig. 8) mainly
452 display most of the bulk susceptibility decrease within 400 to 600 °C, sometimes preceded by
453 a typical of Hopkinson's peak, and mostly reversible heating and cooling curves. These are
454 typical of magnetite and/or titanomagnetite. Most of the thermomagnetic runs (Fig. 8) exhibit
455 a large drop in susceptibility between 400 and 620°C typical of mineralogies dominated by
456 titanomagnetite. In detail, more than one temperature points between 400 and 600 °C, and
457 between 600 and 620 °C, may document a range of titanomagnetite and some titanohematite.
458 However, the strong susceptibility of these phases may hide the potential presence of other
459 iron oxides such as hematite with much lower susceptibility values. AF demagnetizations of
460 these samples typically show that most of the decay occurred between 10 and 60 mT, which
461 is characteristic of magnetite and titanomagnetite. In most samples, the magnetization is fully
462 removed at 100 mT, in others, a significant residual stronger coercivity remanence is
463 preserved above 100 mT (see in particular the Eo–Oligocene and Miocene volcanics and
464 sediments in Figs. 6, and 7). This stronger coercivity is not likely due to goethite not being
465 apparent in the thermal demagnetization. It is rather interpreted to reflect variable occurrences
466 of hematite in the samples. The directions of this high-temperature component, when present
467 in the pilot thermal demagnetizations (Fig. 6 and 7), are indistinguishable from the
468 Characteristic Remanent Magnetization (ChRM) direction defined within 400–600 °C. Further
469 rock-magnetic experiments would be required to better define the precise nature of this
470 occasional high-temperature component. However, this is not necessary for the purpose of
471 our study since this high-temperature component, when present, does not affect the
472 orientation of the well-defined characteristic component carrying most of the magnetization. A
473 more troubling behavior was found upon AF demagnetizations in about 10% and 15% of the
474 Miocene and Eo–Oligocene samples, respectively. In these samples, most of the
475 magnetization was removed after low AF demagnetization within 0-10 mT. This low coercivity
476 may be interpreted to be related to Ti-rich titanomagnetite, which is often present in volcanic
477 rocks outcropping in the region (Dunlop and Ozdemir, 2007; Nugsse et al., 2018). These low
478 coercivity samples have more scattered directions suggesting that some of them have

acquired a recent viscous remagnetization not suitable for further tectonic analyses. To simplify the systematic identification and rejection of these unreliable samples with lower coercivities, the Median Destructive Field (MDF), defined as the applied AF field removing half of the initial magnetization, was used to conservatively reject from further analyses all samples with MDF < 10 mT (Table 2 and Fig. 6c). The three Miocene clastic sedimentary sites had similar behaviors to the surrounding basalts with most of the ChRM demagnetized between 400–600 °C and 20–60 mT (e.g., Fig 7e and f). Given the simple behavior of most basaltic and clastic pilot samples with a Characteristic Remanent Magnetization and well-defined by AF treatment showing univectorial decay towards the origin, this procedure was applied to the bulk of the samples (see Methods). The systematic rejection of samples with low MDF values resulted in discarding five sites that exhibited these behaviors (Table 2).

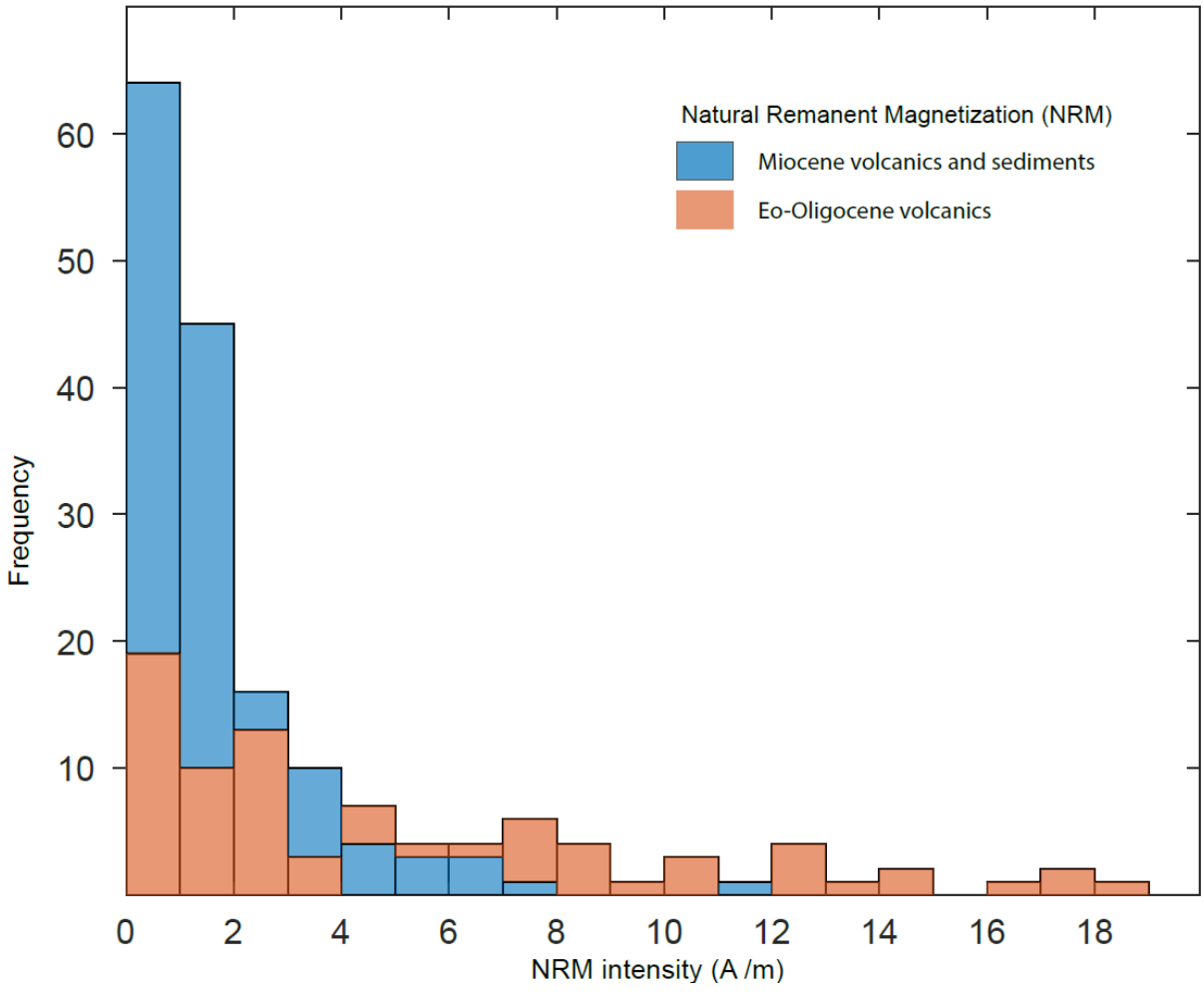

492 Figure 5: Histogram of NRM for the Eo–Oligocene volcanics and the Miocene volcanics and

493 sediments.

Table 2: Sampling location, geologic information,dated rock units and site mean median destructive field (MDF)

Ref.no	ID	Sampling location			Bedding		N	MDF (mT)	Lithology	Age (Ma)	References
		Lat (°)	Lon (°)	Elev (m)	Strike	Dip					
1	CH-1	6.177	37.579	2289	200	5	10	39	Welded tuff	34.1 ± 1.3	Bonini et al., 2005
2	CH-2	6.177	37.579	2289	010	5	9	46	Welded tuff		
3	CH-3[a]	6.256	37.557	2762	010	5	8	7	Basaltic flow	[b]38–36	This study
4	CH-4	6.255	37.541	2762	045	5	8	12	Basaltic flow		
5	SH-1	6.130	37.550	1321	000	0	6	29	Welded tuff		
6	SH-2	6.130	37.520	1325	192	7	4	25	Welded tuff		
7	GE-1	5.909	37.415	1396	000	0	8	13	Basaltic flow	[c]19.62 ± 0.13	This study
8	GE-2	5.909	37.415	1396	000	20	8	15	Basaltic flow		
9	GE-3	5.909	37.416	1409	000	20	8	20	Sediment	15-17	WoldeGabriel et al., 1991
10	GE-4	5.873	37.349	1387	000	0	10	14	Basaltic flow		
11	GE-5	5.873	37.349	1387	000	0	7	46	Basaltic flow		
12	GE-6	6.015	37.270	2556	020	25	7	42	Sediment	15-17	WoldeGabriel et al., 1991
13	GE-7	6.020	37.260	2655	000	0	9	37	Basaltic flow	[c]39.12 ± 0.17	This study
14	GE-8	6.020	37.260	2649	000	0	7	54	Basaltic flow		
15	GE-9	5,955	37.291	2176	000	0	8	37	Basaltic flow		
16	GE-10	5.949	37.288	2048	000	0	8	39	Basaltic flow		
17	GE-11	5.949	37.288	2054	000	0	8	32	Basaltic flow		
18	GE-12	5.949	37.288	2063	000	0	8	21	Basaltic flow	[b]21–19	This study
19	GER-1[a]	5.872	37.350	2730	000	0	9	7	Basaltic flow		
20	GER-2[a]	5.899	37.350	1920	000	0	8	4.2	Basaltic flow	[b]35–32	This study
21	GER-3	6.015	37.269	2542	000	0	10	43	Basaltic flow		
22	KE-1	6.052	37.205	2557	000	0	9	46	Basaltic flow	[d]44.47 ± 0.07	This study
23	KE-2	6.052	37.205	2557	000	0	7	13	Basaltic flow		
24	KE-3	6.046	37.210	2668	000	0	8	34	Basaltic flow		
25	KE-4	6.046	37.210	2668	000	0	5	42	Basaltic flow		
26	KE-5	6.055	37.241	2799	000	0	5	38	Basaltic flow		
27	KE-6	6.052	37.270	2705	000	0	8	30	Basaltic flow		
28	KE-7	6.052	37.270	2705	000	0	7	33	Basaltic flow		
29	KE-8	6.052	37.270	2705	000	0	7	36	Basaltic flow		
30	GD-1	5.643	37.383	1994	210	25	8	13	Sediment	15-17	WoldeGabriel et al., 1991
31	GD-2[a]	5.625	37.397	1695	000	0	8	4	Basaltic flow	[c]39.44 ± 0.15	This study
32	GD-3	5.625	37.397	1695	000	0	8	16	Basaltic flow		
33	KO-1	5,327	37.458	1288	000	0	8	24	Basaltic flow	[c]16.87 ± 0.10	This study
34	KO-2	5.327	37.458	1288	000	0	8	13	Basaltic flow		
35	KO-3[a]	5.315	37.463	1159	000	0	7	8	Basaltic flow		
36	KO-4	5.315	37.463	1159	000	0	5	26	Basaltic flow	[d]35.51 ± 0.10	This study
37	KO-5	5.474	37.329	1785	000	0	7	27	Basaltic flow	18.8 ± 0.7	Ebinger et al., 2000
38	KO-6	5.474	37.329	1785	000	0	7	14	Basaltic flow		
39	MEK-1	6.051	37.270	2694	000	0	7	31	Basaltic flow	[c]38.31 ± 0.07	This study
40	MEK-2	6.065	37.240	2712	000	0	7	12	Basaltic flow	[c]42.44 ± 0.25	This study

Column headings: Ref.no: site reference number; ID, site name; Lat (°), Lon (°) and Elev (m) are locations in latitude, longitude and elevation, respectively. N, number of samples, MDF, site mean destructive field. [a]Sites excluded from further analysis (MDF<10mT). [b]Indicate age range estimated for specific samples from a relatively long flat age patterns comprising >65% fraction of ^{39}Ar release. [c]Indicate plateau age calculated from consecutive heating experiment steps. [d]Indicate total gas age.

494

495

496

497

498

499

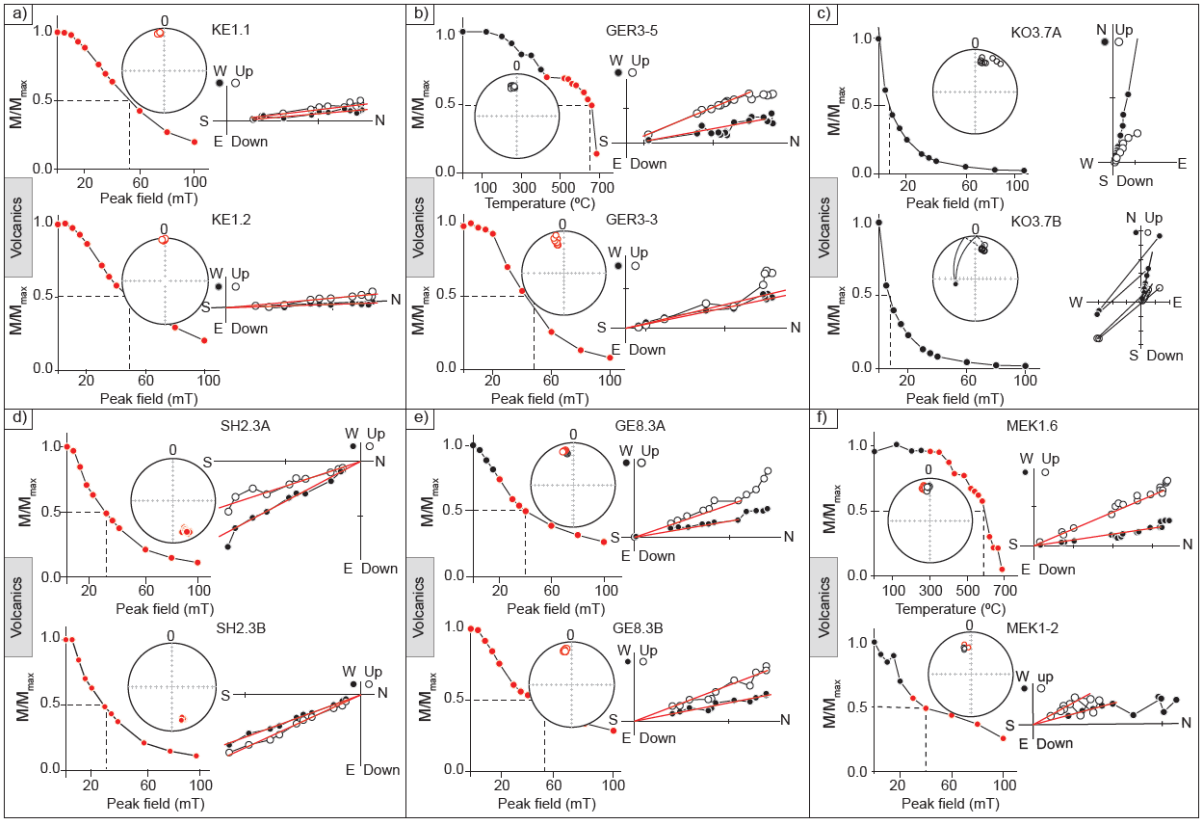

Figure 6. Typical demagnetization behavior of representative specimens obtained from the Eo–Oligocene rocks. Panels (a–f) show stereographic plots, the decay curve exhibiting the median destructive field or temperature (dashed lines), and orthogonal vector end-point diagrams for representative samples demagnetized by AF (a, c, d and e) and thermal treatment (b and f); (c) representative plot for a rejected sample, recording MDF < 10 mT. Red symbols indicate demagnetization steps used for a principal component analysis (red solid line).

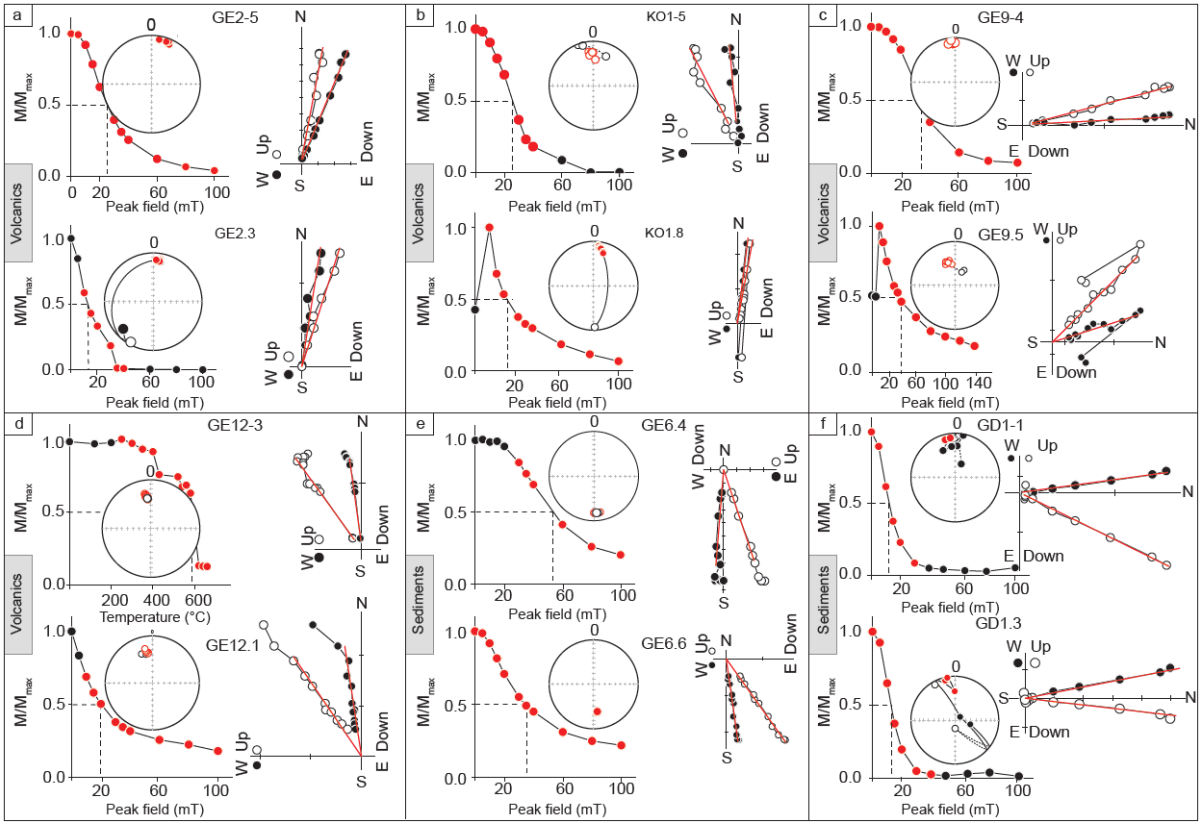

Figure 7. Typical demagnetization behaviors of representative specimens obtained from the Miocene rocks. Panels (a–f) show stereographic plot, the decay curve exhibiting the median destructive field or temperature (dashed lines), and orthogonal vector end-point diagrams for representative samples demagnetized by AF (a–c, e and f) and thermal treatment (d). Red symbols indicate demagnetization steps used for a principal component analysis (red solid line). Most of the specimens exhibit demagnetizations along univectorial paths within 10–60 mT or 400–600 °C (a–e).

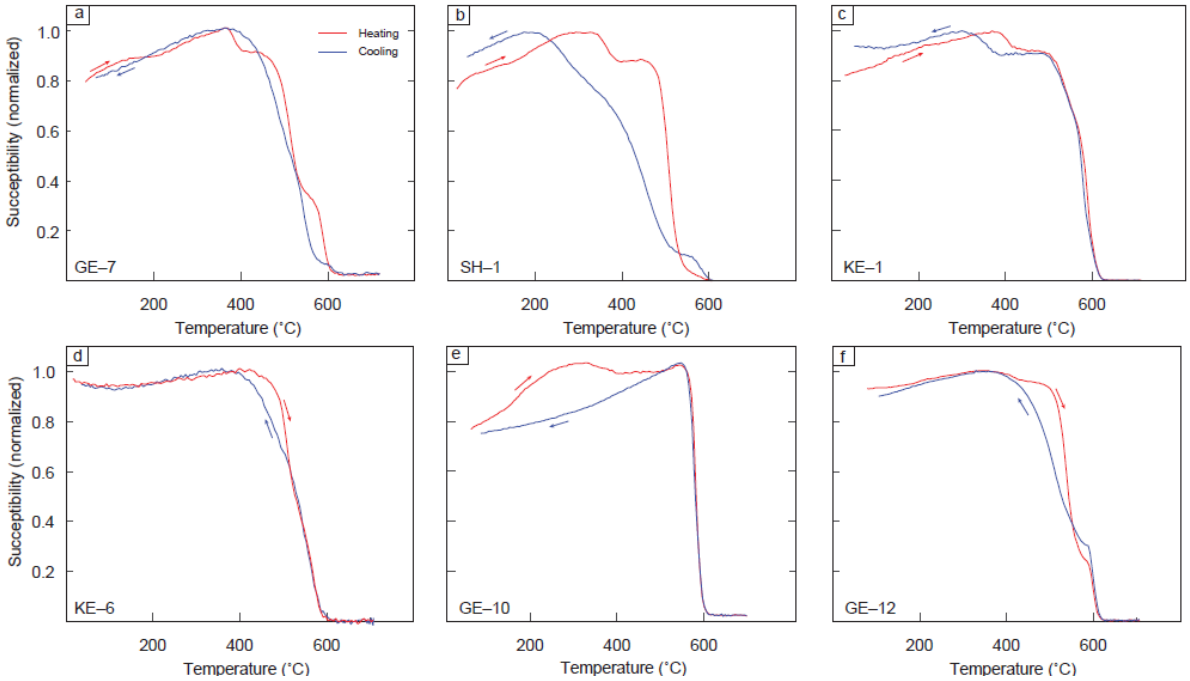

Figure 8: High-temperature thermomagnetic experiment results. Heating (red line) and cooling (blue line) curves for Eo–Oligocene (a–d) and Miocene (e and f) rocks.

3.2.2 Paleomagnetic directions

From the reliable sites, principal component analyses performed on the sample ChRM components yielded well-defined ChRM directions with maximum angular deviations generally well below the threshold value of 15°. These ChRM directions yielded well-defined site-mean directions except for three sites with α_{95} >15° that were discarded (Tables 3 and 4).

In the Eo–Oligocene sites, site means from nearby sites are statistically distinct from each other with 95% confidence. The Eo–Oligocene site-means are generally oriented in normal or reversed polarity orientations after tilt corrections except for three sites widely departing from the mean (Table 3, Fig. 9). These were interpreted as transitional and discarded because the Virtual Geomagnetic Poles (VGP) of these site-means are over 30° from the overall mean paleomagnetic pole of Eo–Oligocene directions (e.g., McFadden et al., 1991). From the remaining sites, a reversals test was positive for the Eo–Oligocene sites based on the overlap within 95% confidence of the mean of the 16 normal and 2 reversed site-mean directions suggesting a primary origin for the ChRM. In addition, the scatter (S=13.2°) in the

distribution of the resulting VGPs is comparable to the expected VGP scatter (S=10-20°) at this latitude from modern global records (Johnson et al., 2008; Deenen et al., 2011) and for the Oligocene to Miocene rocks in Kenya (S=13.8-16.5°; Lhuillier and Gilder, 2019), suggesting the dataset is not undersampling the secular variation. Note that some of the scatter may also result from variable amounts of vertical-axis rotations indistinguishable from the secular variation scatter. Distinguishing between these two sources of scatter is challenging and would require a much larger number of sites to be analyzed. However, undersampling of the secular variation with scatter mainly from rotations is considered unlikely given the observed distribution that exhibits scatter both in inclination and declination, the variations in series of flow sampled at the same locality, and the positive reversals test.

From the Miocene localities, nearby site-mean directions are statistically indistinguishable from each other for three successive basaltic flows (GE-10, 11 and GE-12) dated at 19.8 ± 0.1 Ma. Although they are separated by well-developed flow structures, their indistinguishable magnetization directions suggest that the flows are likely the same or that they were emplaced within a short time interval relative to the rate of geomagnetic secular variation. For this reason, ChRM directions from these flows were combined into a single site-mean. The Miocene site-means record mainly normal polarity directions, except for the samples from site GE-6, which was obtained from sedimentary rock recording both normal and reversed geomagnetic polarity (Table 4). The mean normal direction of Miocene sites is clearly antipodal to this single reversed direction suggesting a primary signal, but the latter being alone prevents us from performing a formal reversals test. The observed scatter (S=18.4) in the distribution of the VGPs derived from these sites is, despite the limited number of sites (N=9), also comparable to the expected VGP scatter at this age and latitude (Johnson et al., 2008; Lhuillier and Gilder, 2019).

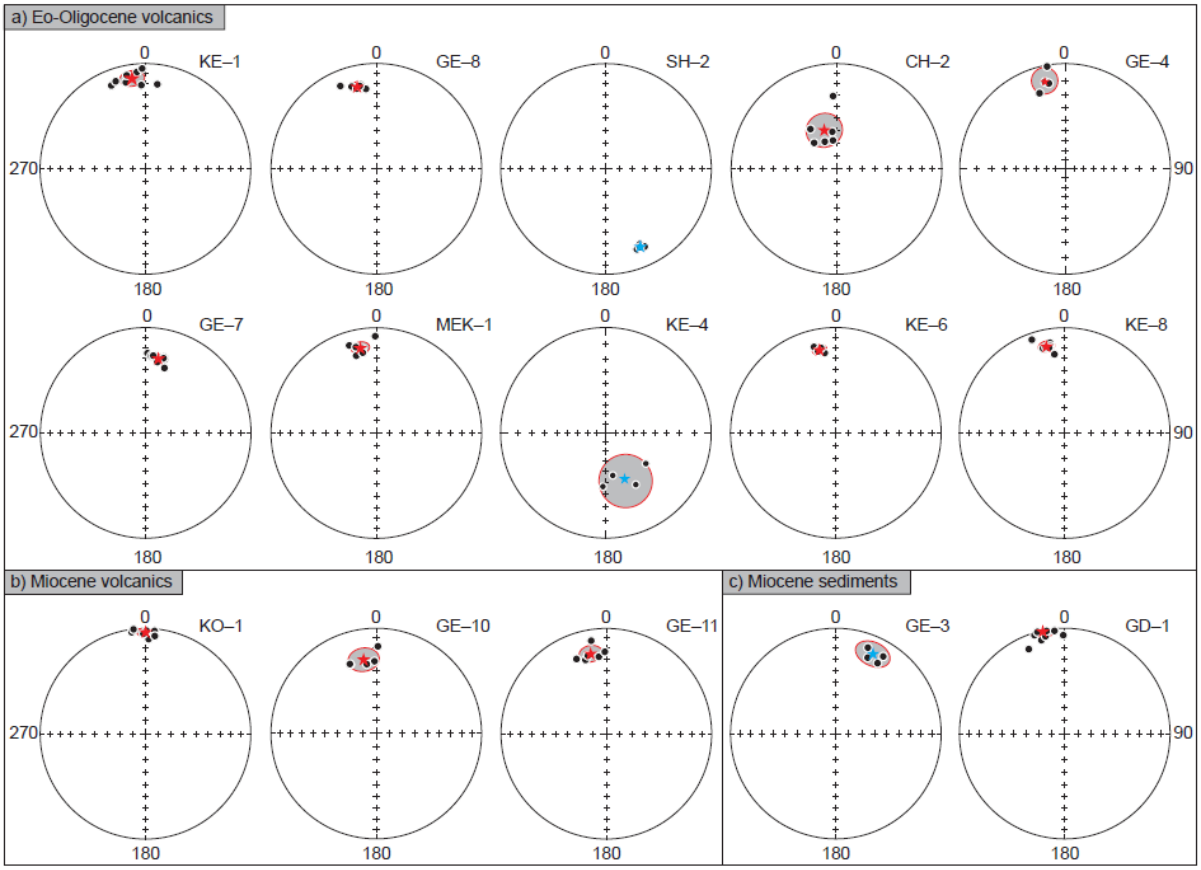

Figure 9: Representative stereoplots of sample ChRM directions at various sites for the Eo–Oligocene volcanics (a) and Miocene volcanics (b) and sediments (c). Site mean directions with 95% (α_{95}) confidence interval are indicated with a star symbol (red and light blue indicate negative and positive inclinations, respectively). Transitional directions SH-2 and KE-4 were excluded when computing an overall mean paleomagnetic direction for the Eo–Oligocene volcanics.

569

Table 3: Paleomagnetic directions and poles for the Eo-Oligocene volcanics sites

ID	N	In Situ		Tilt corrected				Pole			Lithology
		Dg	Ig	Ds	Is	α_{95}	k	ϕ_s	λ_s	α_{95}	
CH-1	5	350.8	-0.9	350.4	-9.7	11.3	27.0	258.7	75.4	11.4	Welded tuff
CH-2[a]	6	339.6	-62.9	342.5	-58.2	13.6	25.3	236.0	42.1	20.1	Welded tuff
CH-4	7	7.6	-16.2	7.6	-16.2	5.2	134.7	189.9	73.6	5.4	Basaltic flow
SH-1	6	169.2	19.4	169.2	19.4	4.9	184.0	251.1	70.5	5.1	Welded tuff
SH-2	4	154.2	23.9	152.1	19.4	3.9	291.0	264.8	63.7	5.5	Welded tuff
GE-4	4	347.0	-9.2	347.0	-9.2	8.3	123.5	268.6	73.3	8.4	Basaltic flow
GE-5[a]	8	291.4	-39.3	291.4	-39.3	3.3	276.1	281.8	17.3	3.9	Basaltic flow
GE-7	8	10.8	-29.6	10.8	-29.6	4.0	232.1	191.3	65.7	4.4	Basaltic flow
GE-8	7	346.8	-21.1	346.8	-21.1	4.6	175.7	255.1	68.6	4.8	Basaltic flow
GER-3	4	351.6	-20.7	351.6	-20.7	6.4	204.3	357.8	80.0	13.1	Basaltic flow
KE-1	8	349.4	-13.1	349.4	-13.1	7.1	73.6	257.2	73.5	7.2	Basaltic flow
KE-2	4	347.3	-21.9	347.3	-21.9	10.9	52.9	253.2	68.5	11.5	Basaltic flow
KE-3	7	8.3	-15.3	8.3	-15.3	11.1	30.6	186.2	73.9	11.4	Basaltic flow
KE-4[b]	4	157.7	39.6	157.7	39.6	23.2	16.6				Basaltic flow
KE-5	5	7.9	-23.9	7.9	-23.9	10.3	57.0	194.3	69.9	11	Basaltic flow
KE-6	4	348.9	-20.7	348.9	-20.7	4.7	386.8	250.7	69.9	4.9	Basaltic flow
KE-7	5	349.0	-18.2	349.0	-18.2	11.1	70.0	252.8	71.1	11.5	Basaltic flow
KE-8	7	348.1	-17.0	348.1	-17.0	5.1	140.0	256.2	71.1	5.3	Basaltic flow
GD-3[a]	5	304.7	8.8	304.7	8.8	3.7	455.0	334.0	79.9	7.0	Basaltic flow
KO-4	5	348.6	16.3	348.6	16.3	10.3	80.6	323.0	78.3	10.6	Basaltic flow
MEK-1	7	349.4	-18.9	349.4	-18.9	5.8	109.8	251.2	71.0	6	Basaltic flow
MEK-2	4	347.5	-20.2	347.5	-20.2	9.0	119.1	254.3	69.3	9.4	Basaltic flow
Mean_N	16	353.5	-16.5	353.6	-16.5	6.0	38.2				
Mean_R	2	161.7	21.8	160.6	19.6	35.8	50.6				
Overall mean[c]	18	352.6	-17	352.6	-17.0	5.5	40.3	243.5	73.5	4.4	

Site name; N, number of samples used to estimate site mean direction; Dg, Ig, Ds and Is, declination and inclination are in situ (g) and tilt-corrected (s); α_{95}, 95% confidence interval; K, precision parameter; ϕs and λs, VGP longitude and latitude, respectively; [a]Transitional directions; [b]sites with α95>15°; [c]An overall mean direction calculated after excluding sites[a and b].

570

Table 4: Paleomagnetic directions and poles for the Miocene volcanics and sediments

Site	N	In Situ		Tilt corrected				Pole			Lithology
		Dg	Ig	Ds	Is	α_{95}	k	ϕ_s	λ_s	α_{95}	
GE-1	7	352.3	24.1	352.3	24.1	10.3	35.3	349.4	79.9	11.0	Basaltic flow
GE-2	4	17.2	1.4	15.8	7.2	8.9	108.0	135.0	74.1	9.0	Basaltic flow
GE-3	4	23.8	14.5	27.1	5.8	10.4	78.3	132.6	62.8	10.4	Sediment
GE-9[a]	7	357.0	-23.6	357.0	-23.6	16.4	12.4				Basaltic flow
GE-10[b]	5	350.3	-29.3	350.3	-29.3	10.5	65.0				
GE-11[b]	6	350.2	-23.3	350.2	-23.3	8.4	54.0				Basaltic flow
GE-12[b]	5	352.7	-33.0	352.7	-33.0	14.3	65.0				Basaltic flow
GD-1	8	345.9	0.6	347.0	-5.1	6.8	67.6	275.4	74.6	6.8	Sediment
KO-1	8	0.1	5.7	0.1	5.7	4.5	153.4	215.1	87.5	4.5	Basaltic flow
KO-2[a]	4	357.9	3.8	357.9	3.8	21.1	20.0				
KO-5	4	13.8	-1.8	13.8	-1.8	14.0	43.8	151.7	74.8	14.0	Basaltic flow
KO-6	2	357.2	-2.5	357.2	-2.5	11.0	521.5	240.0	82.7	11.0	Basaltic flow
GE-6-N[c]	2	354.5	-21.5	354.0	13.0	17.2	213.0				Sediment
GE-6-R[c]	3	176.4	39.4	173.8	4.9	11.3	173.8				Sediment
GE-6[d]	5	175.5	32.2	173.9	2.3	11.0	50.0	268.9	82.2	11.0	Sediment
GE10-12[e]		358.2	-28.7	358.2	-28.7	4.2	73.0	222.1	68.7	4.6	Basaltic flow
Overall Mean[f]	9			2.9	0.9	12.4	18.3	189.7	83.9	9.7	

[a]sites with α95>15°; [b]nearby sites with indistinguishable directions; [c]antipodal polarity directions obtained from a sediment site GE-6; [d]combined mean for antipodal directions from site GE-6; [e]combined mean for sites with indistinguishable directions; [f]overall mean direction calculated after excluding sites[a]. Further details on table column headings can be found in the caption of table 2

571

572

573

574

575

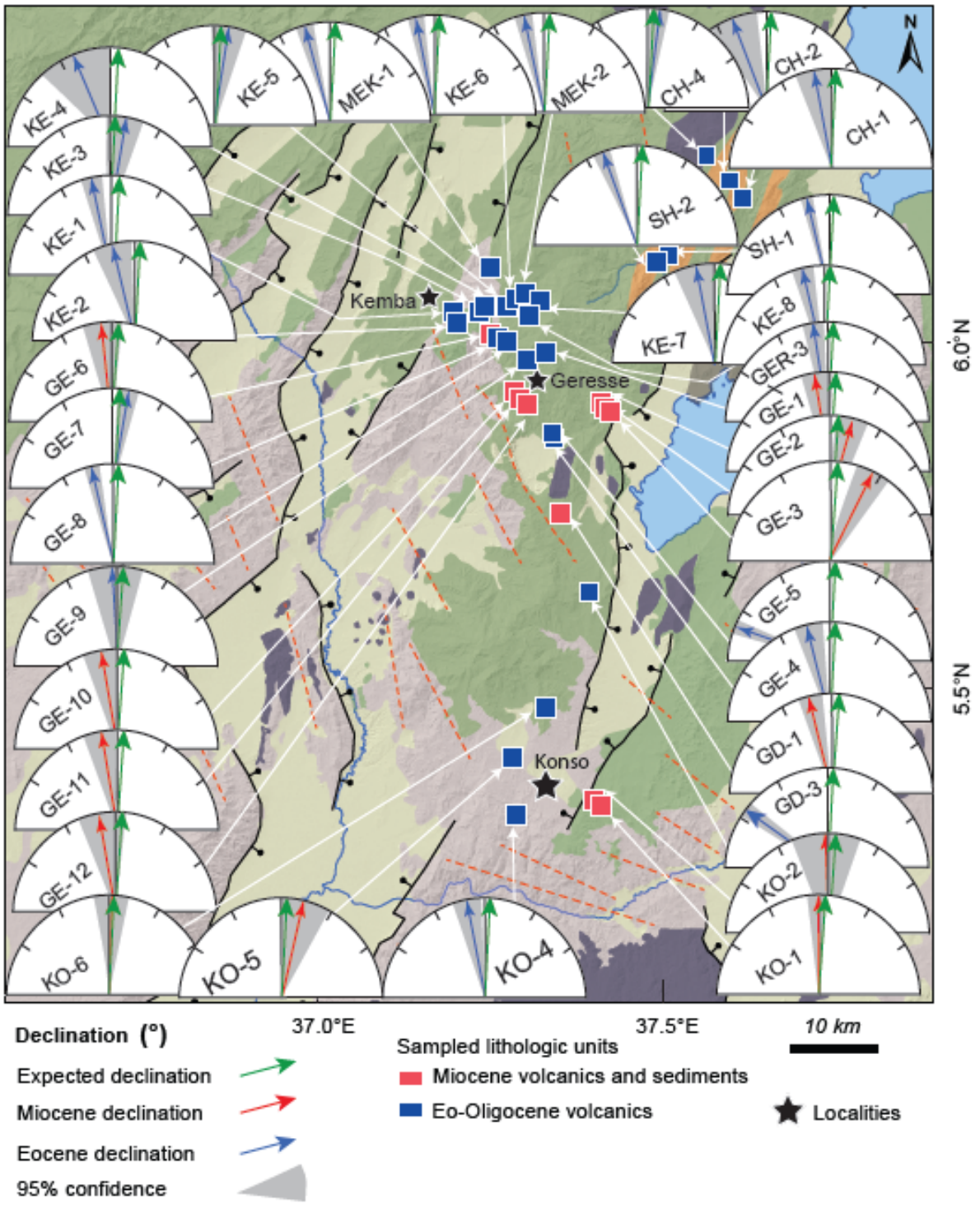

Figure 10: Mean paleomagnetic directions (declination) for each site distributed along and across the Gidole-Chencha Horst superimposed on the sampled stratigraphic units (Davidson, 1983; Bonini et al., 2005) and hill-shaded relief. Squares indicate sampling-site locations of Miocene (red) and Eo–Oligocene (blue) rocks. At each site, the observed mean declination (arrow) is indicated with corresponding 95% confidence interval (gray shaded cone) for the

582 Eo–Oligocene (dark blue) and Miocene (red) rocks. The green arrows indicate the expected
583 direction relative to the pole for Africa at 40 Ma and 20 Ma for sites of Eo–Oligocene and
584 Miocene ages, respectively.

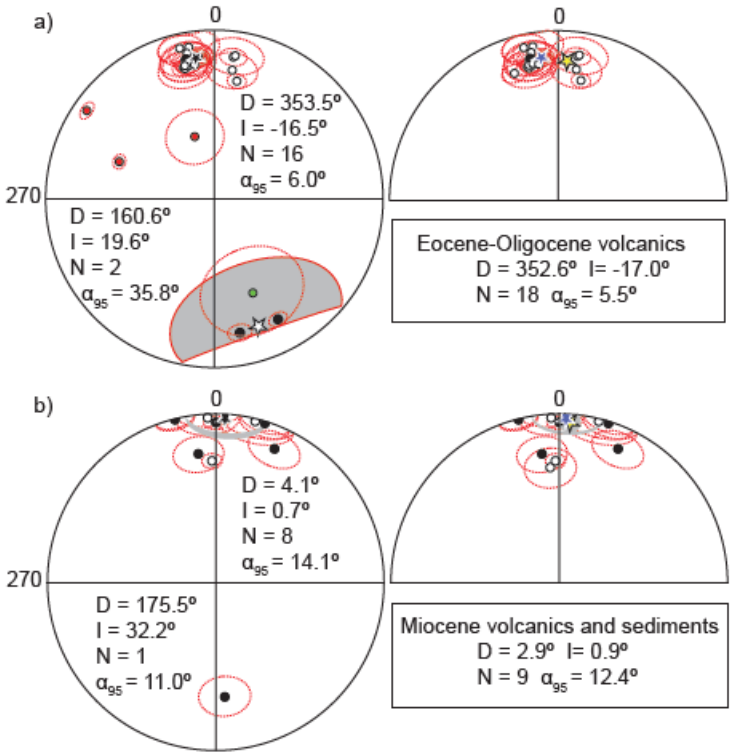

585

586 Figure 11. Stereographic projections of individual site mean direction (circle) with 95%
587 confidence interval (red ellipses). Open (full) symbols are projections on the lower (upper)
588 hemisphere. (a) Eo–Oligocene and (b) Miocene rocks. The black, white, blue and yellow stars
589 in the stereographic projections indicate the mean for normal, reversed, overall mean, and
590 expected directions with the corresponding 95% confidence interval (gray circle or envelope).
591 Excluded site mean directions are shown in full red circles for transitional directions and full
592 green circles for directions recording α_{95}>15.

593 **4 Discussion**

594 **4.1 Vertical-axis tectonic rotations**

595 To interpret the paleomagnetic data from the Eo–Oligocene and Miocene rocks with respect
596 to the tectonic motion of crustal blocks, the obtained directions must be assessed relative to
597 the African reference plate. In our case, the African APWP for the 10 Myr age windows at 40

598 Ma (45–35 Ma; Φ_s=191.6°, λ_s=77.3°, α_{95}=7.2°, N=8) and the 5 Myr age window at 20 Ma
599 (15–20 Ma; Φ_s=165.7°, λ_s=81.7°, α_{95}=4.5°, N=16) provided by Besse and Courtillot (2002)
600 are well suited for our Eo–Oligocene and Miocene groups, respectively. Because of the limited
601 motion of African plate, these (Tauxe, 2005) yield expected inclinations for the studied region
602 nearly indistinguishable for the 40 Ma (Φ_s=172.4°, λ_s=84.3°, α_{95}=3.3°, N=24) and 20 Ma
603 (Φ_s=151.9°, λ_s=85.4°, α_{95}=2.7°, N=38) poles, respectively.

604 A comparison of the observed declination results in map view with the expected
605 declination from the African reference plate (Fig. 10) indicates that the directions of the
606 declinations are not concentrated at a single location; rather, there appear to be small but
607 significant counterclockwise deflections at most Eo–Oligocene sites, reflecting a systematic
608 mechanism that affects the study region. No such trend can be detected at the Miocene sites,
609 which show small variable deflections from the either clockwise or counterclockwise
610 declination expected for the natural dispersion due to the geomagnetic secular variation
611 recorded at those sites.

612 To assess whether the region was affected by statistically significant vertical-axis
613 rotations, the mean paleomagnetic poles (Fig. 11) are compared with the corresponding
614 reference pole. This yielded a significant counterclockwise rotation (13.2° ± 5.9°) of the mean
615 paleomagnetic pole for the Eo–Oligocene sites relative to the 40 Ma and 20 Ma reference
616 poles, respectively (Besse and Courtillot, 1991, 2002), and no significant systematic vertical-
617 axis rotation (3.7° ± 9.3°) for the Miocene sites. We furthermore used the recently developed
618 procedure described in Vaes et al. (2022), available at *www.APWPonline.org*. This procedure,
619 which is based on an improved statistical approach and database, especially with regard to
620 the age of reference poles (see Vaes et al., 2022 for details), generates a reference VGP that
621 is as close as possible to the age of the studied site. The VGP comparison for the Eo–
622 Oligocene sites relative to the paleopoles for stable Africa in the time range between 35 and
623 45 Ma results in a significant counterclockwise rotation of R= 11.1°± 6.4° (Fig. 12a). For the
624 Miocene sites, the observed VGPs in the 11–20 Ma age range relative to the pole for Africa

results in a statistically insignificant vertical-axis rotation (R = 3.2° ± 11.5°; Fig. 12a). The procedure also yields paleolatitudes that are statistically indistinguishable from those expected for Africa at this location during these times (latitudinal displacements L = 2.8° ± 11.5° and L = 4.2° ± 6.2°, respectively, Fig. 12b). These results are averaged over the region and include dispersion from both geomagnetic secular variation and block rotations. The rotations at the Eo–Oligocene sites appear systematic and strong enough to be detected despite the secular variations. However, this is not the case regarding the Miocene sites, recording no statistically significant rotations based on a more limited number of sites. In that case the large 95° confidence interval does not allow us to discard the hypothesis that some smaller (ca. 10°) rotations did not affect the analyzed sites systematically. More data would be required to determine with greater certainty the difference between the age groups or different sub-regions. Nevertheless, with the available data and a careful review of the regional tectonic events first-order interpretations can be derived.

While it is clear that the age of the rotations postdates the emplacement of the Eocene volcanics between 35 and 45 Ma, further ages constraining the rotations are not straightforward. The similarity and regional distribution of the rotations suggest a common underlying mechanism, although we cannot rule out the possibility that the rotations occurred in several phases at different times and locations. The smaller, and statistically insignificant, rotation documented in the Miocene data set (11–20 Ma) indicates that for the most part the rotations recorded by the Eocene volcanics occurred before the emplacement of the Miocene rocks. In light of these observations, we propose two end-member interpretations: either (1) most of the rotation had already occurred by the Miocene, or (2) the rotations have continued continuously until recently. Below, we discuss the potential implication of the vertical-axis rotations with regard to the regional structural setting and models of rift evolution.

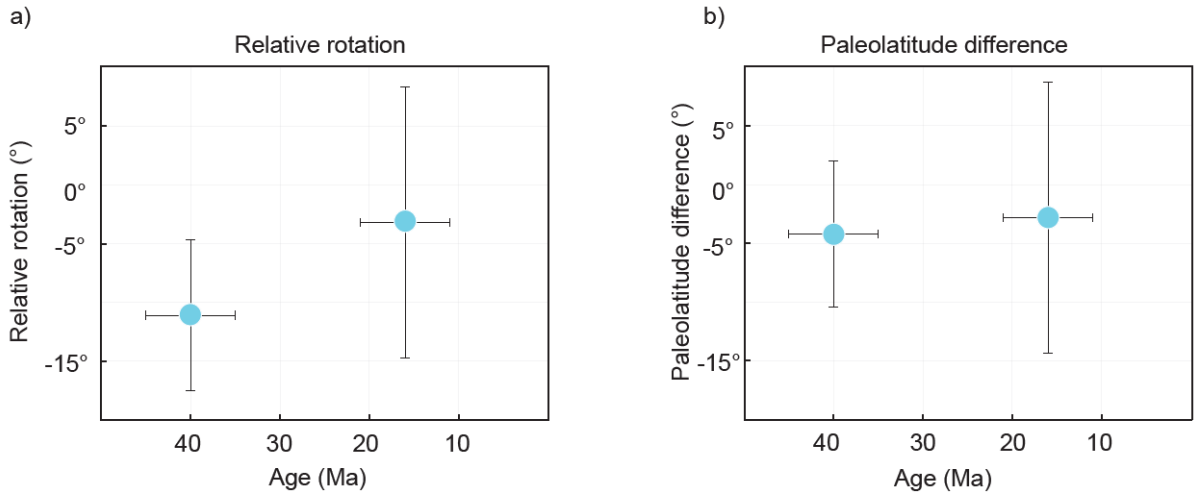

Figure 12. Relative rotation (a) and flattening or latitudinal displacement (b) obtained from comparing the observed Eo–Oligocene and Miocene directions to a reference pole for stable South Africa at a corresponding age range between 35 and 45 Ma (a), and between 11 and 20 Ma (b) (Vaes et al., 2022, 2024).

4.2 Implications for deformation mechanisms

Detected counterclockwise block rotations are consistent with proposed models for the evolution of the southern Main Ethiopian Rift. For example, our results support the expected vertical-axis block rotations that have been suggested in relation to rift overlap between the Chew Bahir Basin-Gofa Province and the southern Main Ethiopian Rift (e.g., Philippon et al., 2014; Brune et al., 2017). Furthermore, the counterclockwise block rotations identified by our analysis support the block-deformation patterns predicted and obtained in analog and numerical modeling studies (Brune et al., 2017; Glerum et al., 2020; Neuharth et al., 2021). Additional insight into the deformation mechanisms can be gained by considering the spatial and temporal characteristics of the extent of vertical-axis block rotation across the overlap zone. By combining our findings with published geologic information from the BRZ, we can further explore and differentiate the temporal variation in the extent of block rotation through two different end-member interpretations of the paleomagnetic data. Our first scenario, which explains the observed vertical-axis rotations by deformation accompanied by

672 counterclockwise block rotation starting between 27 and 20 Ma, synchronous with faulting
673 (e.g., Pik et al., 2008; Erbello et al., 2024), and continuing until the present day. In this model
674 of sustained rotation and deformation, the Eo–Oligocene volcanics would thus record a larger
675 amount of tectonic overprint than the Miocene volcanic and sedimentary sequences. In the
676 second scenario, much of the vertical-axis block rotation would have occurred during the initial
677 rifting phase between 27 and 20 Ma and would have affected the Eo–Oligocene volcanics;
678 however, in this case the region would have only experienced limited block rotations since the
679 late Miocene.

680 This second scenario appears to be more consistent with the regional spatial change
681 in tectonic activity during the Mio–Pliocene (e.g., Davidson, 1983, Ebinger et al., 2000;
682 Chorowicz, 2005; WoldeGabriel et al., 1991; Ebinger et al., 1993, 2000; Bonini et al., 2005;
683 Pik et al., 2008; Philippon et al., 2014, Brune et al., 2017; Boone et al., 2019; Corti et al., 2019;
684 Erbello et al., 2024). Geochronologic, structural, and field data from the southern Main
685 Ethiopian Rift indicate that major faulting along the eastern margin of the Gidole-Chencha
686 Horst occurred between 18 and 14 Ma (Ebinger et al., 2000). Following the development of
687 the marginal fault, deformation migrated toward the Segen Basin and a narrow zone of the
688 southern Main Ethiopian Rift during the middle Miocene and Pliocene, respectively (Levitte,
689 1974; WoldeGabriel et al., 1991; Ebinger et al., 2000; Bonini et al., 2005). West of the Gidole-
690 Chencha Horst along the Gofa Province, a concurrent shift in deformation toward the southern
691 Gofa Province and the Chew Bahir Basin was suggested by WoldeGabriel et al. (1991) and
692 Ebinger et al. (2000). Recent geomorphic investigation of river catchments verified by field
693 observations along the western margin of the Mali-Dancha and Bala-Kela areas in the Gofa
694 Province reveal Quaternary normal faults and young tectonic landforms, suggesting strain
695 localization along a narrow zone in the Gofa Province (Erbello et al., 2022; 2024). The
696 documented spatiotemporal variation in tectonic activity across the BRZ (Philippon et al.,
697 2014; Erbello et al., 2022; 2024) is therefore consistent with the second scenario discussed
698 above. A significant amount of counterclockwise block rotation would have occurred during
699 the early Miocene, mainly prior to the deposition of the Miocene volcanics and sediments,

700 which was superseded by a decrease in block rotation and accompanied by strain localization
701 in the current rift sectors.

702 Finally, our interpretation that rotation ceased in the middle Miocene is consistent with
703 geodetic observations, indicating insignificant present-day block rotation (Knappe et al., 2020).
704 We note, however, that in the first scenario, the observed rotation of 11.1°± 6.4° that has been
705 distributed continuously since 20 Ma, would imply a rotation of ca. 0.5°/Myr, an amount difficult
706 to detect with GPS surveys over such a small region and only spanning a few years or decades.
707 In future studies, a detailed comparison between paleomagnetic data and geodetic
708 observations may lead to more reliable assessments of current deformation patterns involving
709 vertical axis rotations. However, such a comparison would require high-resolution
710 paleomagnetic sampling of Miocene–Holocene volcano-stratigraphic units over an extensive
711 region and a GPS network with sufficient spatial and temporal coverage to detect such small
712 signals.

713

714 **4.3 The role of inherited lineaments in extensional tectonics**

715 In light of the spatiotemporal changes of the locations of volcanism and extension in southern
716 Ethiopia (e.g., Ebinger et al., 2000, Philippon et al., 2014, Corti et al., 2019, Knappe et al.,
717 2020), it is expected that the degree to which tectonic processes reactivated inherited crustal-
718 scale heterogeneities during the Cenozoic has also changed over time. In such a scenario,
719 where vertical-axis rotations involve structural blocks with a diffuse shearing of pre-existing
720 fabrics inherited from previous geodynamic processes (Erbello et al., 2024), it can be inferred
721 that the NW-SE-striking inherited zones of weakness parallel to the rotating blocks may have
722 facilitated lateral motion and efficient kinematic transfer between different rift sectors. For
723 example, the counterclockwise block rotation of ~11 ± 6.4° recorded from the Eo–Oligocene
724 volcanic rocks appears to have decreased significantly over time, as documented by the
725 paleomagnetic signals obtained from the Miocene volcanics. The large extent of vertical axis
726 block rotation might have been facilitated by regional diffuse shear along the NW-SE-oriented

lineaments achieved during early rifting (Boone et al., 2019; Erbello et al., 2024;). However, due to the overall block motion, this process would have later slowed down as the overlapping rift segments would have connected to develop larger, throughgoing extensional structures (e.g., Neuharth et al., 2021). In this context, it is noteworthy that low-temperature thermochronologic data from the Gofa Province record rapid exhumation across the NW-SE-oriented the Beto and Mali-Dancha basin margins during the early Miocene (Boone et al., 2019; Erbello et al., 2024). The reactivation of the NW-SE-striking lineaments during the early Miocene thus likely reflects the role of inherited zones of weakness in facilitating fracture propagation during the initial rifting processes (Fig. 13).

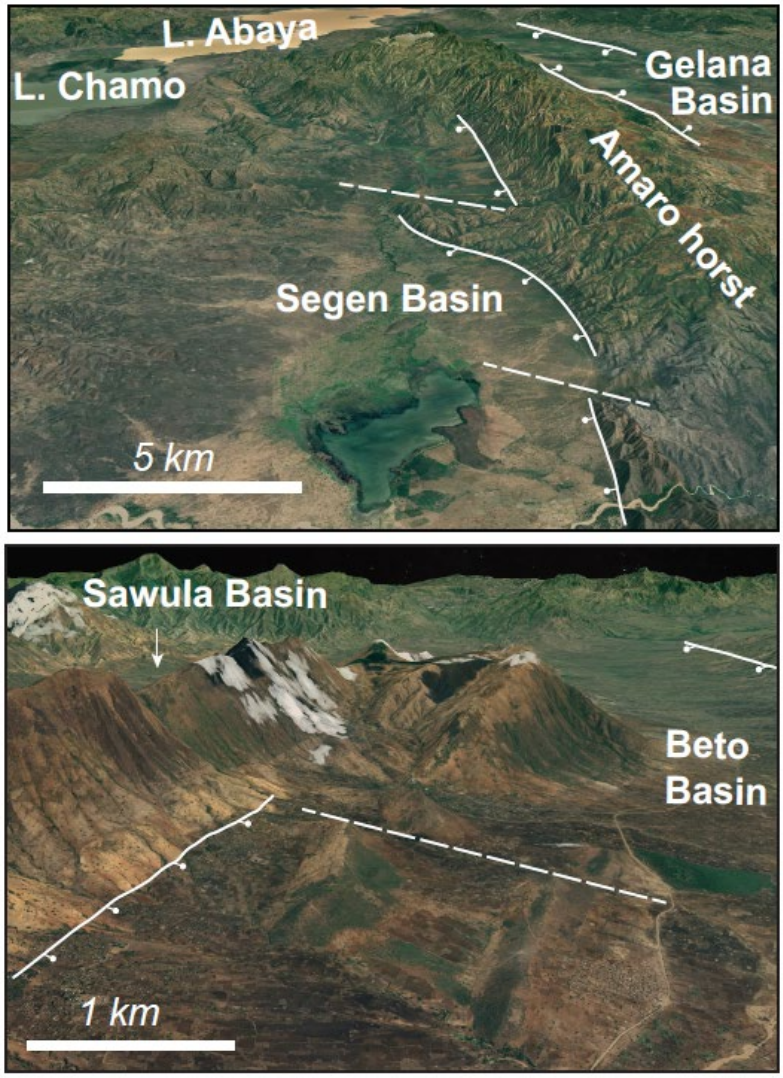

Figure 13. Northwest-view of the southern Main Ethiopian Rift (Segen, Chamo, Gelana, and Abaya basins) and the Gofa Province (Beto and Sawula basins) with basin-bounding faults

(white extended lines with ball and bar symbol). The satellite image is from © Google Earth. The white broken lines indicate NW-SE-striking lineaments with an inferred strike-slip component.

In the context of pre-existing crustal heterogeneities that may facilitate fracture propagation, it is interesting that recent seismic tomographic imaging from the BRZ reveals a near-vertical, NW-SE-trending pervasive band of lineaments below the southern Gofa Province and the northern Chew Bahir Basin (Kounoudis et al., 2021). Additionally, thermochronologic data from this region, obtained at the margin of the Gofa Province, show spatial variations in the onset of faulting and tectonic exhumation (e.g., Balestrieri et al., 2016). Lineaments striking at high angles with respect to the orientation of the rift (Fig. 13), such as the NW-SE-striking reactivated Mesozoic rift-related structures in the BRZ (Bosworth, 1992), may have inhibited meridionally oriented fault propagation and accommodated extensional processes by shearing along these inherited anisotropies (e.g., Molnar et al., 2019).

In line with these observations are earthquake focal mechanism solutions and geological observations that partly indicate a component of horizontal shearing and oblique normal faulting within this Ethiopian extensional province. For example, Asfaw (1990) identified Quaternary oblique-slip faulting along the basin-bounding Chew Bahir and southern Gofa Province faults. Furthermore, earthquakes recorded in the Chew Bahir Basin, the Segen Basin, and more distant regions in the northwestern sector of South Sudan, suggest strike-slip faulting along the NW-SE- and N-S-striking lineaments (Ayele, 2000 and Arvidsson). Finally, a seismicity study in the BRZ and the northern Kenya Rift revealed right-lateral strike-slip faulting in the transition between the southern Main Ethiopian and northern Kenya rifts (Musila et al., 2023; Sullivan et al., 2024). This is consistent with the reactivation of NW-SE-striking lineaments similar to structures depicted in Figures 13 and 14 of our study. The existence of such structures may have facilitated the counterclockwise block rotation between both rift sectors, although lateral displacement along the lineaments appears to have been limited (Fig. 13) (Ebinger et al., 2000).

783

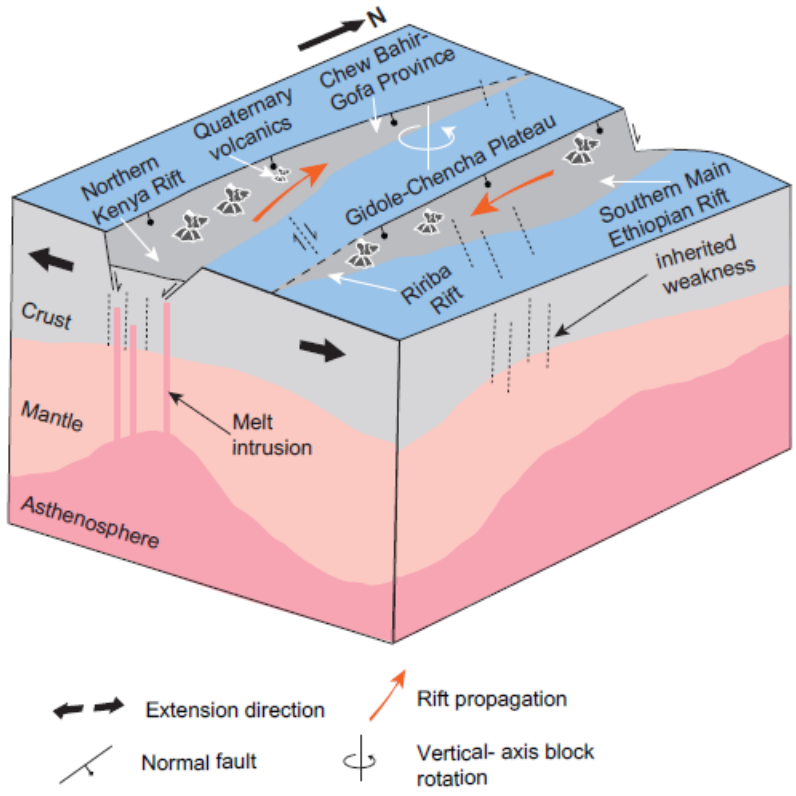

784

785 Figure 14. Oppositely propagating, parallel rift segments and associated vertical axis block
786 rotation across the overlap zone between the southern Main Ethiopian Rift and the Chew Bahir
787 Basin-Gofa Province. The black and orange arrows indicate local plate kinematics (Philippon
788 et al., 2014) and direction of propagating rift segments, respectively. Inferred NW-SE-striking
789 inherited crustal-scale lineaments shown as gray broken lines. The regional-scale model
790 depicting lithospheric structure associated with magmatic intrusions is modified from Ebinger
791 et al. (2000) and Corti (2009).

792

793 **5 Conclusions**

794 Paleomagnetic data combined with published and new $^{40}Ar/^{39}Ar$ data from the ~40-km-wide
795 zone of overlap between the bi-directionally propagating southern Main Ethiopian Rift and the
796 Chew Bahir Basin-Gofa extensional Province reveal a temporal evolution of deformation
797 associated with post–Eocene, approximately 10 to 15° counterclockwise regional vertical-axis
798 block rotations.

799 The combined data set suggests a decrease in the amount of vertical-axis block rotation
800 through time that corresponds well with the migration of deformation toward the axial zone of
801 the southern Main Ethiopian Rift and the extensional Chew Bahir Basin-Gofa Province. In light
802 of regional structural and low-temperature thermochronology data our observations suggest
803 that much of the deformation related to the vertical-axis block rotations likely occurred in the
804 early Miocene, approximately starting between 18 and 14 Ma and progressively decreasing
805 subsequently to a migration of the locus of deformation toward the rift axis during the Pliocene.
806 The pattern of regional counterclockwise block rotations that most likely occurred during
807 early Miocene initial rifting, is inferred to be related to the reactivation of NW-SE-striking
808 Mesozoic lineaments, reflecting the influence of inherited structures on the propagation of
809 fractures and faults during extension. However, further paleomagnetic studies are necessary
810 to ascertain the timing of rotations. The rich volcanic record of southern Ethiopia would provide
811 the opportunity to do this in rare detail. Our study demonstrates the potential of paleomagnetic
812 analyses to constrain tectonic models and quantitatively define the extent of extensional
813 deformation of southern Ethiopia.
814

815 **Acknowledgments**

816 This research was funded by the DAAD through a grant to A. Erbello (German Academic
817 Exchange Service). Additional support came from the Geothermal Development Company,
818 Kenya and funds provided by the Faculty of Mathematics and Natural Sciences of the
819 University of Potsdam to M. Strecker. D. Melnick was funded by the German Research
820 Foundation (DFG), grant ME-3157/4-2. We thank Asfawossen Asrat for having provided us
821 with paleomagnetic sampling equipment. We thank the government offices of Gamo and Gofa
822 for administrative and logistic support. Finally, we would like to thank Ermias Filfilu and Ameha
823 Atnafu Muluneh for their support and H. Pingel for suggestions to improve the illustrations.

824 **Authorship contribution statement**

825 **A. Erbello:** Writing – review & editing, Writing – original draft, Visualization, Software,

826 Methodology, Investigation, Formal analysis, Data curation, Conceptualization.

827 **G. Dupont-Nivet:** Writing – review & editing, Validation, Supervision, Methodology,
828 Investigation, Formal analysis, Conceptualization.

829 **M. R. Strecker:** Writing – review & editing, Validation, Supervision, Methodology,
830 Investigation, Formal analysis, Conceptualization.

831 **T. Kidane:** Writing – review & editing, Validation, Methodology, Conceptualization.

832 **N. Nowaczyk:** Writing – review & editing, Validation, Software, Data curation.

833 **M. Sudo:** Writing – review & editing, Validation, Software, Methodology, Data curation.

834 **D. Melnick:** Writing – review & editing, Validation, Supervision, Conceptualization.

835 **B. Bookhagen:** Writing – review & editing, Visualization, Validation, Supervision,
836 Conceptualization.

837 **S. Brune:** Writing – review & editing, Validation, Conceptualization.

838 **G. Corti:** Writing – review & editing, Validation, Conceptualization.

839 **G. Gecho:** Writing – review & editing, Validation.

840 **Data availability**

841 All the data supporting this research are available in the text and supplementary materials.
842 The supplementary materials can be found at https://doi.org/ 10.5281/zenodo.12247088.
843 Additional data can be found upon request to the corresponding author.

844

845 **6 References**

846 Aanyu, K., and Koehn, D. (2011), Influence of pre-existing fabrics on fault kinematics and rift
847 geometry of interacting segments: Analogue models based on the Albertine Rift
848 (Uganda), Western Branch-East African Rift System. Journal of African Earth Sciences.
849 doi:10.1016/j.jafrearsci.2010.10.003

850 Acocella, V., Morvillo, P., and Funiciello, R. (2005), What controls relay ramps and transfer
851 faults within rift zones? Insights from analogue models. Journal of Structural Geology.
852 doi:10.1016/j.jsg.2004.11.006

853 Acton, G.D., Stein, S., and Engeln, J.F. (1991), Block rotation and continental extension in
854 Afar: A comparison to oceanic microplate systems. Tectonics, doi:10.1029/90TC01792
855 Asfaw, L.M. (1990), Implication of shear deformation and earthquake distribution in the East
856 African Rift between 4°N and 6°N. Journal of African Earth Sciences. doi:10.1016/0899-
857 5362(90)90041-C
858 Ayele, A., and Arvidsson, R. (1997), Fault mechanisms and tectonic implication of the 1985-
859 1987 earthquake sequence in south-western Ethiopia. Journal of Seismology.
860 doi:10.1023/A:1009774331917
861 Balestrieri, M.L., Bonini, M., Corti, G., Sani, F., and Philippon, M. (2016), A refinement of the
862 chronology of rift-related faulting in the Broadly Rifted Zone, southern Ethiopia, through
863 apatite fission-track analysis. Tectonophysics, 671, 42–55.
864 doi:10.1016/j.tecto.2016.01.012
865 Bellahsen, N., Leroy, S., Autin, J., Razin, P., d'Acremont, E., Sloan, H., Pik, R., Ahmed, A., and
866 Khanbari, K. (2013), Pre-existing oblique transfer zones and transfer/transform
867 relationships in continental margins: New insights from the southeastern Gulf of Aden,
868 Socotra Island, Yemen. Tectonophysics. doi:10.1016/j.tecto.2013.07.036
869 Besse, J., and Courtillot, V. (2002), Apparent and true polar wander and the geometry of the
870 geomagnetic field over the last 200 Myr. Journal of Geophysical Research: Solid Earth.
871 doi:10.1029/2000jb000050
872 Besse, J., and Courtillot, V. (1991), Revised and synthetic apparent polar wander paths of the
873 African, Eurasian, North American and Indian plates, and true polar wander since 200
874 Ma. Journal of Geophysical Research. doi:10.1029/90JB01916
875 Bonini, M., Corti, G., Innocenti, F., Manetti, P., Mazzarini, F., Abebe, T., and Pecskay, Z. (2005),
876 Evolution of the Main Ethiopian Rift in the frame of Afar and Kenya rifts propagation.
877 Tectonics. doi:10.1029/2004TC001680
878 Boone, S. C., Balestrieri, M.L., Kohn, B.P., Corti, G., Gleadow, A.J.W., and Seiler, C. (2019),
879 Tectonothermal Evolution of the Broadly Rifted Zone, Ethiopian Rift. Tectonics.
880 doi:10.1029/2018TC005210

881 Boone, Samuel C., Kohn, B.P., Gleadow, A.J.W., Morley, C.K., Seiler, C., Foster, D.A. (2019),
882 Birth of the East African Rift System: Nucleation of magmatism and strain in the Turkana
883 Depression. Geology. doi:10.1130/G46468.1
884 Bosworth, W. (1992), Mesozoic and Early Tertiary rift tectonics in East Africa. Tectonophysics.
885 doi:10.1016/0040-1951(92)90014-W
886 Bosworth, W. (1985), Geometry of propagating continental rifts. Nature.
887 doi:10.1038/316625a0
888 Bosworth, W., and Morley, C.K. (1994), Structural and stratigraphic evolution of the Anza rift,
889 Kenya. Tectonophysics. doi:10.1016/0040-1951(94)90171-6
890 Brune, S., Corti, G., and Ranalli, G. (2017), Controls of inherited lithospheric heterogeneity on
891 rift linkage: Numerical and analog models of interaction between the Kenyan and
892 Ethiopian rifts across the Turkana depression. Tectonics. doi:10.1002/2017TC004739
893 Butler, R.F., 1992. Paleomagnetism: Magnetic Domains to Geologic Terranes. Blackwell,
894 Boston, MA, 319 p.
895 Childs, C., Easton, S.J., Vendeville, B.C., Jackson, M.P.A., Lin, S.T., Walsh, J.J., and
896 Watterson, J. (1993), Kinematic analysis of faults in a physical model of growth faulting
897 above a viscous salt analogue. Tectonophysics. doi:10.1016/0040-1951(93)90346-L
898 Childs, C., Watterson, J., and Walsh, J.J. (1995), Fault overlap zones within developing normal
899 fault systems. Journal of the Geological Society of London. doi:10.1144/gsjgs.152.3.0535
900 Chorowicz, J. (2005), The East African rift system. Journal of African Earth Sciences.
901 doi:10.1016/j.jafrearsci.2005.07.019
902 Chu, D., and Gordon, R.G. (1999), Evidence for motion between Nubia and Somalia along the
903 Southwest Indian Ridge. Nature. doi:10.1038/18014
904 Cogne, J.P. (2003), PaleoMac: A Macintosh™ application for treating paleomagnetic data and
905 making plate reconstructions. Geochemstry, Geophysics, Geoszstems, 4(1), 1-8.
906 doi:10.1029/2001GC000227, 2003.
907 Corti, G. (2008), Control of rift obliquity on the evolution and segmentation of the Main
908 Ethiopian Rift. Nature Geoscience. doi:10.1038/ngeo160

909 Corti, G., Cioni, R., Franceschini, Z., Sani, F., Scaillet, S., Molin, P., Isola, I., Mazzarini, F.,
910 Brune, S., Keir, D., Erbello, A., Muluneh, A., Illsley-Kemp, F., and Glerum, A. (2019),
911 Aborted propagation of the Ethiopian rift caused by linkage with the Kenyan rift. Nature
912 Communications, 10. doi:10.1038/s41467-019-09335-2
913 Cox, A. (1973), Tectonics and Geomagnetic Reversals. W.H. Freeman, San Francisco, CA,
914 p. 702 p
915 Dawers, N.H., and Anders, M.H. (1995), Displacement-length scaling and fault linkage.
916 Journal of Structural Geology. doi:10.1016/0191-8141(94)00091-D
917 Deenen, M.H., Langereis, C.G., van Hinsbergen, D.J., and Biggin, A.J. (2011), Geomagnetic
918 secular variation and the statistics of paleomagnetic directions. Geophysical Journal
919 International doi:10.1111/j.1365-246X.2011.05050.x
920 DeMets, C., Merkouriev, S., and Sauter, D. (2015), High-resolution estimates of Southwest
921 Indian Ridge plate motions, 20 Ma to present. Geophysical Journal International.
922 doi:10.1093/gji/ggv366
923 Dommain, R., Riedl, S., Olaka, L.A., DeMenocal, P., Deino, A.L., Owen, R.B., Muiruri, V.,
924 Müller, J., Potts, R., and Strecker, M.R. (2022), Holocene bidirectional river system along
925 the Kenya Rift and its influence on East African faunal exchange and diversity gradients.
926 Proceedings of the National Academy of Sciences 119. doi:10.1073/pnas.2121388119
927 Dunlop, D.J., Özdemir, O. (1997), Rock Magnetism: Fundamentals and Frontiers. Cambridge
928 University Press, Cambridge 573 p.
929 Ebinger, C., and Scholz, C.A. (2012), Continental Rift Basins: The East African Perspective.
930 in: Busby, C., Azor, A. (Eds.), Tectonics of Sedimentary Basins: Recent Advances.
931 doi:10.1002/9781444347166.ch9
932 Ebinger, C.J., Jackson, J.A., Foster, A.N., and Hayward, N.J. (1999), Extensional basin
933 geometry and the elastic lithosphere. Philosophical Transactions of the Royal Society A:
934 Mathematical, Physical and Engineering Sciences. doi:10.1098/rsta.1999.0351
935 Ebinger, C.J., Yemane, T., Harding, D.J., Tesfaye, S., Kelley, S., and Rex, D.C. (2000), Rift
936 deflection, migration, and propagation: Linkage of the Ethiopian and Eastern rifts, Africa.

937 Bulletin of the Geological Society of America. doi:10.1130/0016-
938 7606(2000)112<163:RDMAPL>2.0.CO;2
939 Ebinger, C.J., Yemane, T., Woldegabriel, G., Aronson, J.L., and Walter, R.C. (1993), Late
940 Ecocene-Recent volcanism and faulting in the southern main Ethiopian rift. Journal of the
941 Geological Society of London. doi:10.1144/gsjgs.150.1.0099
942 Emishaw, L., and Abdelsalam, M.G. (2019), Development of Late Jurassic-Early Paleogene
943 and Neogene-Quaternary rifts within the Turkana Depression, East Africa from satellite
944 gravity data. Tectonics, 38, 2358–2377. doi:10.1029/2018TC005389
945 Erbello, A., and Kidane, T. (2018), Timing of volcanism and initiation of rifting in the Omo-
946 Turkana depression, southwest Ethiopia: Evidence from paleomagnetism. Journal of
947 African Earth Sciences. doi:10.1016/j.jafrearsci.2017.12.031
948 Erbello, A., Melnick, D., Zeilinger, G., Bookhagen, B., Pingel, H., and Strecker, M.R. (2022),
949 Geomorphic expression of a tectonically active rift-transfer zone in southern Ethiopia.
950 Geomorphology. doi:10.1016/j.geomorph.2022.108162
951 Erbello, A., Colleps, C., Melnick, D., Sobel, E.R., Bookhagen, B., Pingel, H., Zeilinger, G., van
952 der Beek, P., and Strecker, M.R. (2024), Magma-assisted continental rifting: The broadly
953 rifted zone of SW Ethiopia, East Africa. Tectonics. doi:10.1029/2022TC007651
954 Erbello. A., Dupont-Nivet. G., Kidane. T., Nowaczyk. N., Sudo. M., Melnick. D., Bookhagen.
955 B., Brune. S., Corti. G., Gecho. G., and Strecker, M.R. (2023), Temporal variation in
956 counterclockwise vertical-axis block rotations across a rift overlap zone, southwestern
957 Ethiopia, East Africa [data set]. Zenodo. doi: 10.5281/zenodo.8263190
958 Fernandes, R.M.S., Miranda, J.M., Delvaux, D., Stamps, D.S., and Saria, E. (2013), Re-
959 evaluation of the kinematics of the Victoria block using continuous GNSS data.
960 Geophysical Journal International. doi:10.1093/gji/ggs071
961 Fisher, R. (1953), Dispersion on a sphere. Proceedings of the Royal Society A: Mathematical,
962 Physical and Engineering Sciences. doi:10.1098/rspa.1953.0064
963 Faccenna, C., Glišović, P., Forte, A., Becker, T.W., Garzanti, E., Sembroni, A., and Gvirtzman,
964 Z. (2019), Role of dynamic topography in sustaining the Nile River over 30 million years.

965 Nature Geoscience. doi:10.1038/s41561-019-0472-x
966 Fleck, R. J., J. F. Sutter and D. H. Elliot (1977): Interpretation of discordant $^{40}Ar/^{39}Ar$ age-
967 spectra of Mesozoic tholeiites from Antarctica. Geochimica et Cosmochimica Acta, 41,
968 15-32
969 Franceschini, Z., Cioni, R., Scaillet, S., Corti, G., Sani, F., Isola, I., Mazzarini, F., Duval, F.,
970 Erbello, A., Muluneh, A., and Brune, S. (2020), Recent volcano-tectonic activity of the
971 Ririba rift and the evolution of rifting in South Ethiopia. Journal of Volcanology and
972 Geothermal Research. doi:10.1016/j.jvolgeores.2020.106989
973 Garcin, Y., Melnick, D., Strecker, M.R., Olago, D., and Tiercelin, J.-J. (2012), East African mid-
974 Holocene wet–dry transition recorded in palaeo-shorelines of Lake Turkana, northern
975 Kenya Holocene wet–dry transition recorded in palaeo-shorelines of Lake Turkana,
976 northern Kenya. Earth Planet. Sci. Lett. 331–332, 322–334. doi.org/
977 10.1016/j.epsl.2012.03.016.
978 Glerum, A., Brune, S., Stamps, D.S., and Strecker, M.R. (2020), Victoria continental microplate
979 dynamics controlled by the lithospheric strength distribution of the East African Rift.
980 Nature Communications. doi:10.1038/s41467-020-16176-x
981 Gouin, P. (1979), Earthquake History of Ethiopia and the Horn Of Africa. Geophysical
982 Observatory,University of Addis Ababa, Addis Ababa.
983 Halama, R., M. Konrad-Schmolke, M. Sudo, H. Marschall and M. Wiedenbeck (2014): Effects
984 of fluid-rock interaction on $^{40}Ar/^{39}Ar$ geochronology in high-pressure rocks (Sesia-Lanzo
985 Zone, Western Alps). Geochimica et Cosmochimica Acta, 126, 475-494
986 Hetzel, R., and Strecker, M.R. (1994), Late Mozambique Belt structures in western Kenya and
987 their influence on the evolution of the Cenozoic Kenya Rift. Journal of Structural Geology.
988 doi:10.1016/0191-8141(94)90104-X
989 Johnson, C.L., Constable, C.G., Tauxe, L., Barendegt, R., Brown, L.L., Coe, R.S, and Stone,
990 D.B. (2008), Recent investigations of the 0–5 Ma geomagnetic field recorded by lava
991 flows. Geochemistry, Geophysics, Geosystems. doi:10.1029/2007GC001696
992 Katz, R.F., Ragnarsson, R., and Bodenschatz, E. (2005), Tectonic microplates in a wax model

993 of sea-floor spreading. New Journal of Physics. doi:10.1088/1367-2630/7/1/037
994 Kidane, T., Courtillot, V., Manighetti, I., Audin, L., Lahitte, P., Quidelleur, X., Gillot, P.-Y., Gallet,
995 Y., Carlut, J., and Haile, T. (2003), New paleomagnetic and geochronologic results from
996 Ethiopian Afar: Block rotations linked to rift overlap and propagation and determination of
997 a ~2 Ma reference pole for stable Africa. Journal of Geophysical Research: Solid Earth.
998 doi:10.1029/2001jb000645
999 Kidane, T., Otofuji, Y.I., Komatsu, Y., Shibasaki, H., and Rowland, J. (2009), Paleomagnetism
1000 of the Fentale magmatic segment, Main Ethiopian Rift: New evidence for
1001 counterclockwise block rotation linked to transtensional deformation. Physics of the Earth
1002 and Planetary Interiors. doi:10.1016/j.pepi.2009.04.006
1003 Kirschvink, J.L. (1980), The least-squares line and plane and the analysis of palaeomagnetic
1004 data. Geophysical Journal of the Royal Astronomical Society. doi:10.1111/j.1365-
1005 246X.1980.tb02601.x
1006 Knappe, E., Bendick, R., Ebinger, C., Birhanu, Y., Lewi, E., Floyd, M., King, R., Kianji, G.,
1007 Mariita, N., Temtime, T., Waktola, B., Deresse, B., Musila, M., Kanoti, J., and Perry, M.
1008 (2020), Accommodation of East African rifting across the Turkana Depression. Journal of
1009 Geophysical Research: Solid Earth. doi:10.1029/2019JB018469
1010 Koehn, D., Aanyu, K., Haines, S., and Sachau, T. (2008), Rift nucleation, rift propagation and
1011 the creation of basement micro-plates within active rifts. Tectonophysics.
1012 doi:10.1016/j.tecto.2007.10.003
1013 Kolawole, F., Firkins, M.C., Al Wahaibi, T.S., Atekwana, E.A., and Soreghan, M.J. (2021), Rift
1014 interaction zones and the stages of rift linkage in active segmented continental rift
1015 systems. Basin Research 33. doi:10.1111/bre.12592
1016 Koukouvelas, I.K., Asimakopoulos, M., and Doutsos, T.T. (1999), Fractal characteristics of
1017 active normal faults: An example of the eastern Gulf of Corinth, Greece. Tectonophysics.
1018 doi:10.1016/S0040-1951(99)00087-6
1019 Kounoudis, R., Bastow, I.D., Ebinger, C.J., Ogden, C.S., Ayele, A., Bendick, R., Mariita, N.,
1020 Kianji, G., Wigham, G., Musila, M., and Kibret, B. (2021), Body-wave tomographic

imaging of the Turkana Depression: Implications for rift development and plume-lithosphere interactions. Geochemistry, Geophysics, Geosystems. doi:10.1029/2021GC009782

Lee, J-Y., Marti, K., Severinghaus, J.P., Kawamura, K., Yoo, H-S., Lee, J.B., and Kim, J.S. (2006), A redetermination of the isotopic abundances of atmospheric Ar. Geochimica et Cosmochimica Acta, 70, 4507-4512. doi: 10.1016/j.gca.2006.06.1563

Levitte, D., Columba, J., and Mohr, P. (1974), Reconnaissance geology of the Amaro Horst, southern Ethiopian Rift. Geological Society of America Bulletin. doi:10.1130/0016-7606(1974)85<417:RGOTAH>2.0.CO;2

MacDonald, K.C., and Fox, P.J. (1983), Overlapping spreading centres: New accretion geometry on the East Pacific Rise. Nature. doi:10.1038/302055a0

McKenzie, D., and Jackson, J. (1986), A block model of distributed deformation by faulting. Journal of the Geological Society. doi:10.1144/gsjgs.143.2.0349

Michael Kendall, J., and Lithgow-Bertelloni, C. (2016), Why is Africa rifting?, in: Journal of the Geological Society Special Publication. doi:10.1144/SP420.17

Molnar, N.E., Cruden, A.R., and Betts, P.G. (2019), Interactions between propagating rifts and linear weaknesses in the lower crust. Geosphere. doi:10.1130/GES02119.1

Moore, J.M., and Davidson, A. (1978), Rift structure in southern Ethiopia. Tectonophysics. doi:10.1016/0040-1951(78)90111-7

Morgan, L.E., D.F. Mark, J. Imlach, D. Barfod, R. Dymock (2014): FCs-EK: a new sampling of the Fish Canyon Tuff $^{40}Ar/^{39}Ar$ neutron flux monitor. Jourdan, F., Mark, D.F. & Verati, C. (eds.) 2014. Advances in $^{40}Ar/^{39}Ar$ Dating: from Archaeology to Planetary Sciences. Journal of the Geological Society Special Publication, 378, 63-67

Morley, C.K., Nelson, R.A., Patton, T.L., and Munn, S.G. (1990), Transfer zones in the East African Rift System and their relevance to hydrocarbon exploration in rifts. American Association of Petroleum Geologists Bulletin. doi:10.1306/0c9b2475-1710-11d7-8645000102c1865d

Morley, C.K., Wescott, W.A., Stone, D.M., Harper, R.M., Wigger, S.T., and Karanja, F.M.

(1992), Tectonic evolution of the northern Kenyan Rift. Journal of the Geological Society . doi:10.1144/gsjgs.149.3.0333

Muluneh, A.A., Kidane, T., Rowland, J., and Bachtadse, V. (2013), Counterclockwise block rotation linked to southward propagation and overlap of sub-aerial Red Sea Rift segments, Afar Depression: Insight from paleomagnetism. Tectonophysics. doi:10.1016/j.tecto.2013.02.030

Musila, M., C. J. Ebinger, I. D. Bastow, G. Sullivan, S. J. Oliva, E. Knappe, M. Perry, R. Kounoudis, C. S. Ogden, R. Bendick, S. Mwangi, N. Mariita, G. Kianji, E. Klein, F. Illsley-Kemp (2023), Active deformation constraints on the Nubia-Somalia Plate Boundary through Heterogeneous Lithosphere of the Turkana Depression, Geochemistry, Geophysics, Geosystems. doi: 10.1029/2023GC0109822023GC010982

Nelson, R.A., Patton, T.L., and Morley, C.K. (1992), Rift-segment interaction and its relation to hydrocarbon exploration in continental rift systems. American Association of Petroleum Geologists Bulletin. doi:10.1306/bdff898e-1718-11d7-8645000102c1865d

Neuharth, D., Brune, S., Glerum, A., Helne, C., and Welford, J.K. (2021), Formation of continental microplate through rift linkage: numerical modeling and its application to the Flemish Cap and Sao Paulo Plateau. Geochemistry, Geophysics, Geosystems. doi:10.1029/2020GC009615

Nugsse, K., Muluneh, A.A., and Kidane, T. (2018), Paleomagnetic evidence for counterclockwise rotation of the Dofan magmatic segment, Main Ethiopian Rift. Tectonophysics. doi10.1016/j.tecto.2018.03.013

Olaka, L.A., Kasemann, S.A., Sültenfuß, J., Wilke, F.D.H., Olago, D.O., Mulch, A., and Musolff, A. (2022), Tectonic control of groundwater recharge and flow in faulted volcanic aquifers. Water Resources Research. doi:10.1029/2022WR032016

Peacock, D.C.P. (2002), Propagation, interaction and linkage in normal fault systems. Earth-Science Reviews. doi:10.1016/S0012-8252(01)00085-X

Philippon, M., Corti, G., Sani, F., Bonini, M., Balestrieri, M.L., Molin, P., Willingshofer, E., Sokoutis, D., and Cloetingh, S. (2014), Evolution, distribution, and characteristics of rifting

in southern Ethiopia. Tectonics. doi:10.1002/2013TC003430

Pik, R., Marty, B., Carignan, J., Yirgu, G., and Ayalew, T. (2008), Timing of East African Rift development in southern Ethiopia: Implication for mantle plume activity and evolution of topography. Geology. doi:10.1130/G24233A.1

Ragon, T., Nutz, A., Schuster, M., Ghienne, J.F., Ruffet, G., and Rubino, J.L. (2019), Evolution of the northern Turkana Depression (East African Rift System, Kenya) during the Cenozoic rifting: New insights from the Ekitale Basin (28-25.5 Ma). Geological Journal. doi:10.1002/gj.3339

Renne, P.R., G. Balco, K.R. Ludwig, R. Mundil and K. Min (2011): Response to the comment by W.H. Schwarz et al. on "Joint determination of ^{40}K decay constants and $^{40}Ar^*/^{40}K$ for the Fish Canyon sanidine standard, and improved accuracy for $^{40}Ar/^{39}Ar$ geochronology" by P.R. Renne et al. (2010). Geochimica et Cosmochimica Acta.

Rooney, T.O. (2010), Geochemical evidence of lithospheric thinning in the southern Main Ethiopian Rift: Lithos, v. 117, p. 33–48, https:// doi .org /10 .1016 /j.lithos .2010 .02 .002

Rooney, T.O. (2017), The Cenozoic magmatism of East-Africa: Part I. Flood basalts and pulsed magmatism. Lithos, 286-287, 264-301. doi: 10.1016/j.lithos.2017.05.014

Rosendahl, B.R. (1987), Architecture of continental rifts with special reference to East Africa. Annual Review of Earth and Planetary Sciences. doi:10.1146/annurev.earth.15.1.445

Saria, E., Calais, E., Altamimi, Z., Willis, P., and Farah, H. (2013), A new velocity field for Africa from combined GPS and DORIS space geodetic Solutions: Contribution to the definition of the African reference frame (AFREF). Journal of Geophysical Research: Solid Earth. doi:10.1002/jgrb.50137

Saria, E., Calais, E., Stamps, D.S., Delvaux, D., and Hartnady, C.J.H. (2014), Present-day kinematics of the East African Rift. Journal of Geophysical Research: Solid Earth. doi:10.1002/2013JB010901

Schouten, H., Klitgord, K.D., and Gallo, D.G. (1993), Edge-driven microplate kinematics. Journal of Geophysical Research: Solid Earth. doi:10.1029/92jb02749

Schaen, A.J., Jicha, B.R., Hodges, K.V., Vermeesch, Stelten, M.E., Mercer et al. (2020),

1105 Interpreting and reporting Ar-Ar geochronologic data. Geological Society of America
1106 Bulletin. doi:10.1130/B35560.1
1107 Stamps, D.S., Calais, E., Saria, E., Hartnady, C., Nocquet, J.M., Ebinger, C.J., and Fernandes,
1108 R.M. (2008). A kinematic model for the East African Rift. Geophysical Research Letters.
1109 doi:10.1029/2007GL032781
1110 Stamps, D.S., Saria, E., and Kreemer, C. (2018), A geodetic strain rate model for the East
1111 African Rift System. Scientific Reports. doi:10.1038/s41598-017-19097-w
1112 Steiner, R.A., Rooney, T.O., Girard, G., Rogers, N., Ebinger, C.J., Peterson, L., and Phillips,
1113 R.K. (2021), Initial Cenozoic magmatic activity in East Africa: new geochemical
1114 constraints on magma distribution within the Eocene continental flood basalt province, in:
1115 Journal of the Geological Society . doi:10.1144/SP518-2020-262
1116 Sullivan, G., Ebinger, C.J., Musila, M., Perry, M., , Kraus, E.R., Bastow, I., Bendick, B. (2024),
1117 Kinematics of rift linkage between the Eastern and Ethiopian rifts in the Turkana
1118 Depression, Africa. Basin Research, 36 (5). https://doi.org/10.1111/bre.12900
1119 Tauxe, L. (2005), Inclination flattening and the geocentric axial dipole hypothesis. Earth and
1120 Planetary Science Letters. doi:10.1016/j.epsl.2005.01.027
1121 Tauxe, L., Kent, D.V. (1982), A time framework based on magnetostratigraphy for the Siwalik
1122 sediments of the Khaur area, northern Pakistan. Paleogeography Palaeoclimatology.
1123 Paleoecology. doi:10.1016/0031-0182(82)90057-8.
1124 Tauxe, L. (2005), Inclination flattening and the geocentric axial dipole
1125 hypothesisdoi:10.1016/j.epsl.2005.01.027
1126 Uto, K., O. Ishizuka, A. Matsumoto, H. Kamioka and S. Togashi (1997): Laser-heating $^{40}Ar/^{39}Ar$
1127 dating system of the Geological Survey of Japan: System outline and preliminary results.
1128 Bulletin of the Geological Survey of Japan, 48, 23-46
1129 Vaes, B., Gallo, L.C., and van Hinsbergen, D.J. J. (2022), On Pole Position: Causes of
1130 dispersion of the paleomagnetic poles behind Apparent Polar Wander Paths. Journal of
1131 Geophysical Research, Solid Earth. doi: 10.1029/2022JB023953
1132 Vaes, B., van Hinsbergen, D., & Paridaens, J. (2024), APWP-online.org: a Global Reference

Database and Open-Source Tools for Calculating Apparent Polar Wander Paths and Relative Paleomagnetic Displacements. тектоніка, 2(1), 174–189. doi:10.55575/tektonika2024.2.1.44

Versfelt, J., and Rosendahl, B.R. (1989), Relationships between pre-rift structure and rift architecture in Lakes Tanganyika and Malawi, East Africa. Nature (337), 354-357.

Wilke, F.D.H., P.J. O'Brien, A. Gerdes, M.J. Timmerman, M. Sudo and M.A. Khan (2010): The multistage exhumation history of the Kaghan Valley UHP series, NW Himalaya, Pakistan from U-Pb and $^{40}Ar/^{39}Ar$ ages. European Journal of Mineralogy, 22, 703-719

Woldegabriel, G., Aronson, J.L., and Walter, R.C. (1990), Geology, geochronology, and rift basin development in the central sector of the Main Ethiopia Rift. Bulletin of the Geological Society of America. doi:10.1130/0016-7606(1990)102<0439:GGARBD>2.3.CO;2

WoldeGabriel, G., Yemane, T., Suwa, G., White, T., and Asfaw, B. (1991), Age of volcanism and rifting in the Burji-Soyoma area, Amaro Horst, southern Main Ethiopian Rift: geo- and biochronologic data. Journal of African Earth Sciences. doi:10.1016/0899-5362(91)90107-A